Radiative sensitivity quantified by a new set of radiation flux kernels based on the ERA5 reanalysis

Han Huang, Yi Huang

Department of Atmospheric and Oceanic Sciences, McGill University, Montreal, Canada

Corresponding Authors:

Han Huang, han.huang2@mcgill.ca (ORCID: 0000-0002-9143-6453),

Yi Huang, yi.huang@mcgill.ca (ORCID: 0000-0002-5065-4198)

19 **Abstract**

21 Radiative sensitivity, i.e., the response of the radiative flux to climate perturbations, is essential
22 to understanding climate change and variability. The sensitivity kernels computed by radiative
23 transfer models have been broadly used for assessing the climate forcing and feedbacks for
24 global warming. As these assessments are largely focused on the top of atmosphere (TOA)
25 radiation budget, less attention has been paid to the surface radiation budget or the associated
26 surface radiative sensitivity kernels. Based on the fifth generation European Center for Medium-
27 Range Weather Forecasts (ERA5) atmospheric reanalysis, we produce a new set of radiative
28 kernels for both the TOA and surface radiative fluxes, which is made available at
29 http://dx.doi.org/10.17632/vmg3s67568.3 (Huang and Huang, 2023). By comparing with other
30 published radiative kernels, we find that the TOA kernels are generally in agreement in terms of
31 global mean radiative sensitivity and analyzed overall feedback strength. The unexplained
32 residual in the radiation closure tests is found to be generally within 10% of the total feedback,
33 no matter which kernel dataset is used. The uncertainty in the TOA feedbacks caused by inter-
34 kernel differences, as measured by the standard deviation of the global mean feedback parameter
35 value is much smaller than the inter-climate model spread of the feedback values. However, we
36 find relatively larger discrepancies in the surface kernels. The newly generated ERA5 kernel
37 outperforms many other datasets in closing the surface energy budget, achieving a radiation
38 closure comparable to the TOA feedback decomposition, which affirms the validity of kernel
39 method for the surface radiation budget analysis. In addition, by investigating the ERA5 kernel
40 values computed from the atmospheric states of different years, we notice some apparent
41 interannual differences, which demonstrates the dependence of radiative sensitivities on the
42 mean climate state and partly explains the inter-dataset kernel value differences. In this paper, we
43 provide a detailed description on how ERA5 kernels are generated and considerations to ensure
44 proper use of them in feedback quantifications.

45

46

47

1. Introduction

Radiative kernels measure the sensitivity of radiative fluxes to the perturbation of feedback variables, such as temperature, water vapor, albedo and cloud (e.g., Soden and Held, 2006; Huang et al., 2007; Shell et al., 2008; Previdi, 2010; Zelinka et al., 2012; Block and Mauritsen, 2013; Yue et al., 2016; Huang et al., 2017; Pendergrass et al., 2018; Thorsen et al., 2018; Kramer et al., 2019b; Smith et al., 2020). Compared to the partial radiative perturbation method (e.g., Wetherald and Manabe, 1988), which is precise but computationally expensive, the kernel method deploys a set of precalculated radiative kernels with simple arithmetic multiplications in feedback quantification and thus is computationally highly efficient, which has greatly facilitated the analysis of radiative feedbacks in global climate models (GCM) (e.g., Soden and Held, 2006; Soden et al., 2008; Jonko et al., 2012; Vial et al., 2013; Zhang and Huang, 2014; Dong et al., 2020; Zelinka et al., 2020; Chao and Dessler, 2021), as well as in observations (e.g., Dessler, 2010; Kolly and Huang, 2018; Zhang et al., 2019; Huang, H. et al., 2021). These analyses have helped dissect and understand the climate sensitivity differences among the GCMs, such as those in Coupled Model Intercomparison Projects, CMIP5 (Taylor et al., 2012) and CMIP6 (Eyring et al., 2016). For example, Zelinka et al. (2020) attributed the higher climate sensitivity in the CMIP6 models to their more positive extratropical cloud feedback. The kernel-enabled feedback analyses have also provided insights in the energetics of the climate variations such as the El Nino and Southern Oscillation (ENSO, e.g., Dessler et al., 2010; Kolly & Huang 2018; Huang et al. 2021a), the Madden-Julian Oscillation (MJO, e.g., Zhang et al. 2019) and the Arctic sea ice interannual variability (e.g., Huang et al., 2019), despite the approximate nature of the kernel method and the known limits of its accuracy (e.g., Colman and Mcavaney, 1997; Huang and Huang, 2021).

Multiple sets of radiative kernels have been developed to date, using different radiation codes and based on different atmospheric state datasets ranging from GCMs to global reanalysis and satellite datasets, for both non-cloud variables (e.g., Soden and Held, 2006; Shell et al., 2008; Huang et al., 2017; Thorsen et al., 2018; Bright and O'halloran, 2019; Donohoe et al., 2020) and cloud properties (e.g., Zelinka et al., 2012; Zhou et al., 2013; Yue et al., 2016; Zhang et al., 2021; Zhou et al., 2022). As the conventional feedback analyses are mostly concerned with the radiation energy budget change at the TOA, most existing kernels have been developed and tested to address that need, i.e., to measure the feedback contributions to the TOA radiation changes. Although the radiative sensitivity depends on the atmospheric states as well as the radiative transfer codes used to compute the kernel values (e.g., Collins et al., 2006; Huang and Wang, 2019; Pincus et al., 2020), it has been noted that the global mean TOA feedback quantification is insensitive to which kernel dataset is used, as the diagnosed feedback values are close to each other when measured by different kernel datasets (e.g., Soden et al., 2008; Jonko et al., 2012; Vial et al., 2013; Zelinka et al., 2020). However, as there is increasing interest in regional climate change and associated feedback (e.g., Kolly and Huang, 2018; Huang et al., 2019; Zhang et al. 2019), it becomes important to know how the kernels (dis)agree at regional scales. The generation of the global radiative kernels usually requires radiative transfer computation based on a large number of instantaneous atmospheric profiles. Due to this computational cost, many kernel datasets are generated based on the atmospheric data from an arbitrary calendar year. Given the known interannual climate differences, e.g., between El Niño to La Niña years, this warrants investigations to ascertain whether the kernels may differ in important ways for regional feedback assessments.

94   On the other hand, fewer feedback studies have addressed the surface radiation budget,
95   although its importance has been recognized for such problems as the precipitation change
96   (Previdi, 2010; Pendergrass and Hartmann, 2014; Myhre et al., 2018) and oceanic energy
97   transport (e.g., Zhang and Huang, 2014; Huang et al., 2017). The surface budget analysis
98   requires the use of surface kernels, which are not always available from the published kernel
99   datasets. Few of them have been subject to inter-comparisons or rigorous validation. As
100 explained below in this paper, the computation and use of them require different care than the
101 TOA kernels. Possibly due to the lack of such recognition, there exist considerable discrepancies
102 between the existing surface kernels and some surface budget-centered analyses reported
103 alarmingly large non-closure in their radiation budget analyses (e.g., Vargas Zeppetello et al.,
104 2019), calling into question the validity of kernel method for surface radiation budget analysis.
105 Hence, we are motivated to examine the radiative sensitivity quantified by different kernels,
106 especially for the surface budget.
107   In this work, we produce a new set of radiative kernels for both the TOA and surface
108 radiation fluxes based on the fifth generation European Center for Medium-Range Weather
109 Forecasts atmospheric reanalysis (ERA5, Hersbach et al., 2020), which demonstrates superior
110 accuracy in the quantification of various atmospheric states (e.g., Graham et al., 2019; Wright et
111 al., 2020), and document the key considerations in the kernel computation procedure. We
112 intercompare the kernels computed from ERA5 to the other previously generated ones, and
113 investigate the interannual variation of the kernel values due to their atmospheric state
114 dependency. In addition, applying a selected set of kernels to analyzing the feedback in the
115 CMIP6 models, we intercompare the discrepancies in quantified feedbacks across the GCMs and
116 across different kernels.
117
118
119 **2. Construction of ERA5 radiative kernels**
120
121 **2.1 Radiative transfer model and atmospheric dataset**
122
123   We use the GCM version of the rapid radiative transfer model (RRTMG) (Mlawer et al.,
124 1997) to calculate the radiative kernels. RRTMG conducts radiative transfer calculations in 16
125 longwave (LW) spectral bands and 14 shortwave (SW) bands. The accuracy of this model has
126 been extensively validated against the line-by-line calculations (e.g., Collins et al, 2006).
127   Input data required by RRTMG, including surface pressure, skin temperature, air
128 temperature, water vapor, albedo, ozone concentration, cloud fraction, cloud liquid water content
129 and cloud ice content, are taken from the instantaneous (as opposed to monthly mean) data of the
130 ERA5 reanalysis, with a horizontal resolution of 2.5 degree by 2.5 degree and 37 vertical
131 pressure levels between 1 hPa and 1000 hPa. To ensure the accuracy of radiative kernels in upper
132 atmosphere (Smith et al., 2020), we patch five layers of the U.S. standard profile above 1 hPa in
133 the LW calculations. Other required input variables, such as the effective radii of cloud liquid
134 droplet and ice crystal are taken from the 3-hourly synoptic TOA and surface fluxes and cloud
135 product of the Clouds and Earth's Radiant Energy System (CERES) (Doelling et al., 2013) with
136 a horizontal resolution of 1 degree and then interpolated to the same resolution as the ERA5 data
137 (2.5 degree). A random cloud overlapping scheme is used in our all-sky calculation. Sensitivity
138 tests have been conducted to determine the necessary temporal sampling for a proper
139 representation of the diurnal cycle and 6-hourly and 3-hourly instantaneous profiles are adopted

140   for LW and SW radiative transfer calculations, respectively, to limit the root mean squared error
141   of the computed diurnal mean flux biases to less than one percent.
142
143
144   **2.2 Radiative kernel computation**
145
146   Radiative kernels in essence measure the change of radiative flux to unit perturbation of
147   atmospheric variables, i.e., $\frac{\partial R}{\partial X}$, where R is either the upwelling irradiance flux at the TOA or
148   upwelling/downwelling irradiance flux at the surface; X represents the aforementioned feedback
149   variables; K_X is the radiative kernel of variable X. Note that for each radiative flux, K_X varies
150   with the time, geographic and vertical locations of the perturbed variable and is in general a 4-
151   dimensional (4-D) data array. Note also that all radiative fluxes and kernel values are defined as
152   downward positive.
153   Following the previous studies, we compute non-cloud radiative kernels including the LW
154   kernels of surface temperature (T_s), air temperature (T_a), and water vapor ($WV\ LW$), and the SW
155   kernels of surface albedo (ALB) and water vapor ($WV\ SW$). To calculate the kernels, we use the
156   partial radiative perturbation experiments, conducting two radiative transfer computations, one
157   without perturbation (control run) and the other with a perturbation of one atmospheric variable;
158   the difference between these two computations is used to calculate the radiative kernel value. In
159   both experiments, the upward, downward and net radiative fluxes at the TOA and surface are
160   saved at each time instance and location. Then ΔR_0 can be obtained by differencing the saved
161   radiative fluxes between the perturbed and unperturbed experiments. Dividing ΔR_0 with the
162   perturbation of variable X (ΔX_0), the instantaneous radiative kernel K_X is calculated as
163

$$K_X = \frac{\Delta R_0}{\Delta X_0} \qquad (1)$$

164
165
166   Applying such perturbation computations to all the relevant variables (see Appendix for a
167   detailed discussion of the procedure), we obtain instantaneous radiative kernels of these
168   dimensionalities: the surface temperature and albedo kernels are 3-D arrays (time, latitude|73,
169   longitude|144), and the air temperature and water vapor kernels are 4-D arrays (time, level|37,
170   latitude|73, longitude|144).
171   To account for possible interannual variability of the radiative kernel values, we compute
172   the kernels using atmospheric data of five calendar years: from year 2011 to 2015. Among these
173   years, 2011 is a strong La Niña year, 2015 is a strong El Niño year. Monthly or annual mean
174   kernels are then averaged from the instantaneous computations. For example, the LW annual
175   mean kernel of 2011 is obtained as $K = \frac{1}{365*4}\sum_{i=1}^{365*4} K_i$ (365 is the number of days of a year and
176   4 is because 6-hourly data are used for LW calculations) and the SW kernels, $K =$
177    $\frac{1}{365*8}\sum_{i=1}^{365*8} K_i$ (8 is because 3-hourly data are used for SW calculations), where the index i
178   represents the time slices included in the averaging. Similar averaging procedure is applied to
179   monthly mean kernels. The analyses in this work are based on multi-year averaged monthly
180   mean kernels if not otherwise stated.
181
182   **3. Characterization of ERA5 kernels**
183

184
185
186   In this section, we first present the all-sky TOA and surface radiative sensitivity kernels
187 quantified from the ERA5 in Figure 1 to 4 (see the clear-sky kernels in Figure S1 and S2). The
188 atmospheric radiation flux kernels, i.e., the change in radiation flux convergence in the
189 atmosphere due to the perturbation of feedback variables and measured by differencing TOA and
190 surface kernels, are shown in Figure S3 and S4 for interested readers. Then, we compare ERA5
191 kernels with the other kernel datasets and we examine the interannual variability of the ERA5
192 kernel values, due to the dependency of radiative sensitivity on the background atmospheric
193 state.
194
195 **3.1 Distribution of radiative sensitivity**
196
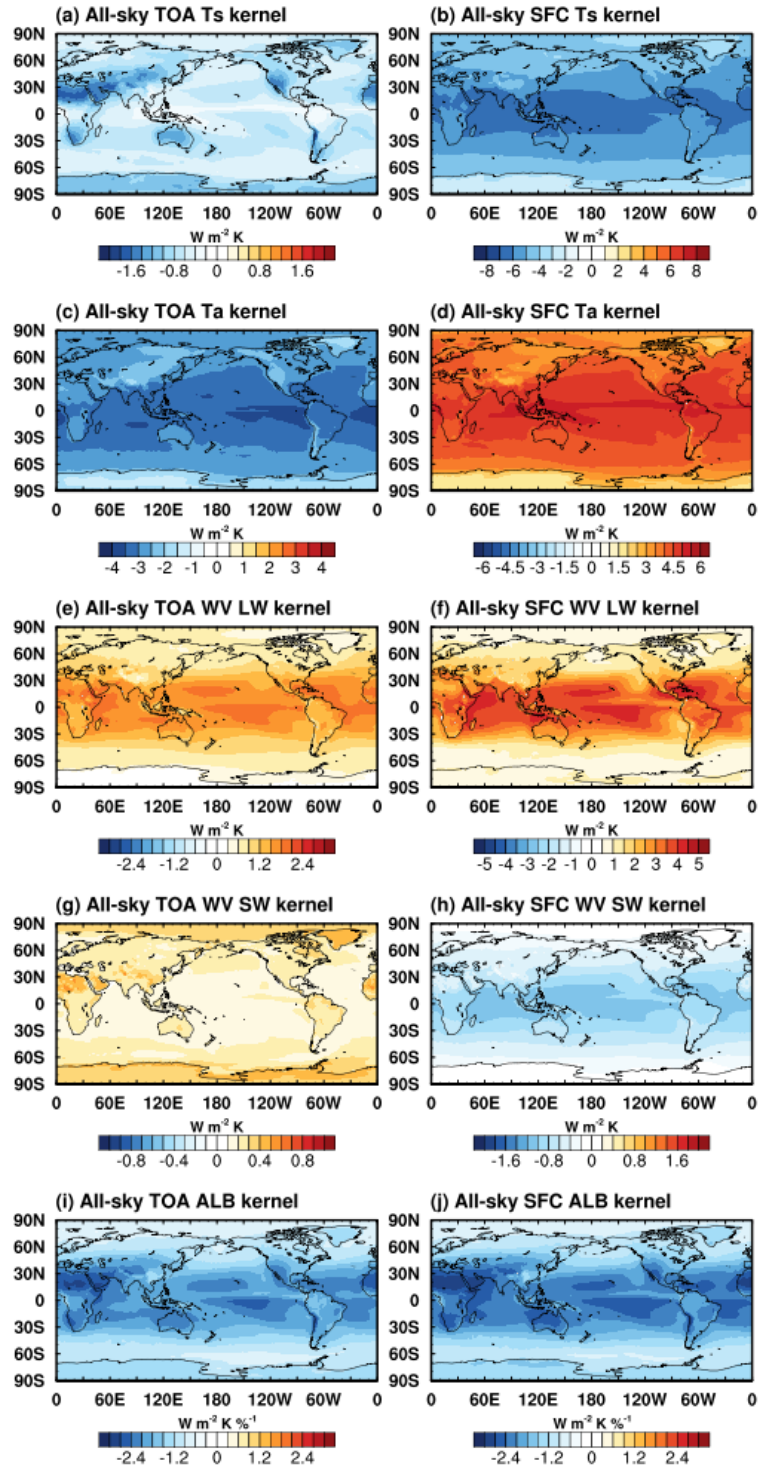
Figure 1. All-sky (left) TOA and (right) surface ERA5 kernels of (a, b) surface temperature (T_s), (c, d) air temperature (T_a), (e, f) water vapor longwave ($WV\ LW$), (g, h) water vapor shortwave ($WV\ SW$) and (i, j) surface albedo (ALB). Note that for T_a, $WV\ LW$, and $WV\ SW$ kernels, vertically integrated values are shown, which represents the sensitivity of radiative flux to a whole-column atmospheric perturbation. Note that the colorbar ranges differ among panels.

204

205   Figure 1 summarizes the spatial distribution of all-sky ERA5 kernels for TOA and surface
206   and Figure 2 illustrates the vertical cross-sections of zonal mean air temperature, water vapor
207   LW and water vapor SW kernels in all-sky (see Figure S1 and S2 for results in clear-sky). For
208   surface temperature kernel, an increase of surface temperature leads to more upwelling longwave
209   radiation (i.e., OLR) both at the surface and TOA, therefore the kernel is negative. The TOA flux
210   sensitivity in clear-sky (Figure S1a) is stronger than that in all-sky (Figure 1a) due to the absence
211   of cloud, and the value increases with latitude, due to the decreasing concentration of water
212   vapor from the tropics to the poles. The all-sky TOA sensitivity is strongly influenced by clouds,
213   showing, for example, the fingerprint of the ITCZ in the tropical oceans (Figure 1a). The
214   locations with less atmospheric absorption due to less water vapor or cloud, e.g., in the Tibetan
215   Plateau and Sahara Desert regions, show relatively stronger sensitivity (Figure 1a). For the
216   surface flux kernels, the increase of surface temperature enhances the upward emission
217   according to the Planck function and thus the distribution follows that of surface temperature in
218   both clear-sky and all-sky (Figure 1b).

219   For air temperature kernel, the increase of air temperature increases the OLR at TOA and
220   also the downwelling flux at surface, so the TOA and surface kernels take negative and positive
221   signs, respectively. The TOA kernel has maximum values in the tropics, due to the higher air
222   temperature (Planck function) and more abundant cloud and water vapor (higher emissivity)
223   there, and generally decreases in magnitude with latitude (Figure 1c). Unlike the TOA flux
224   kernel, which shows comparable sensitivity to air temperature at nearly all vertical levels, the
225   surface flux is mainly sensitive to the bottom layers (Figure 2b).

226   For water vapor LW kernel, an increase of water vapor reduces OLR at TOA and increases
227   downwelling radiation at surface, so that the TOA and surface kernels are both positive in sign.
228   The vertically integrated kernel values (Figure 1e and f) generally follow the temperature
229   distribution, for example, decreasing in magnitude with latitude. In both cases, the kernel
230   magnitude is dampened by clouds in all-sky. The vertically resolved kernels show maximum
231   sensitivity of TOA flux to the upper troposphere (Figure 2c) and maximum sensitivity of surface
232   flux to the bottom layers (Figure 2d), respectively. In terms of the atmospheric radiation (the
233   convergence of the TOA and surface radiation fluxes in the atmosphere), the increase in water
234   vapor concentration absorbs more LW in the upper troposphere than what it emits but the
235   opposite is true in the lower troposphere (Figure S4c). Such features were discussed in previous
236   works (e.g., Huang et al. 2007).

237   For water vapor SW kernel, an increase of water vapor absorbs solar radiation and thus
238   reduces both the upwelling (reflected) SW flux at TOA and the downwelling SW flux at surface.
239   As a result, the two kernels take positive and negative signs, respectively. Note the magnitude of
240   the SW kernels is much weaker than that of the LW kernels, because water vapor absorbs the
241   LW flux more significantly than the SW flux. One noticeable feature of the TOA kernel in clear-
242   sky (Figure S1g) is that the magnitude over the land is stronger than that over the ocean, because
243   the relatively higher albedo over the land reflects more SW radiation and thus enhances the
244   absorption by the water vapor in the atmosphere. For this reason, over reflective surfaces such as
245   the Sahara Desert and Tibetan Plateau, as well as the Poles, the sensitivity is maximized. Unlike
246   the TOA kernel, the distribution of surface kernel follows the distribution of background water
247   vapor concentration, with noticeable dampening by clouds (Figure 1h and 2f).

248   For surface albedo kernel, an increase of surface albedo leads to more upwelling
249   (reflected) SW flux both at surface and TOA; therefore, the kernel is of negative sign. In clear-

250 sky, the sensitivity strength follows the pattern of solar insolation, with some local maxima, e.g.,
251 in the Sahara Desert and Tibetan Plateau (Figure S1i and j) due to the relatively lower water
252 vapor concentration. In all-sky, the distribution is again influenced by cloud patterns; for
253 example, in the ITCZ region, the strength is much reduced as clouds reduce the solar radiation
254 reaching the surface and thus the sensitivity to surface albedo change (Figure 1i and j).
255
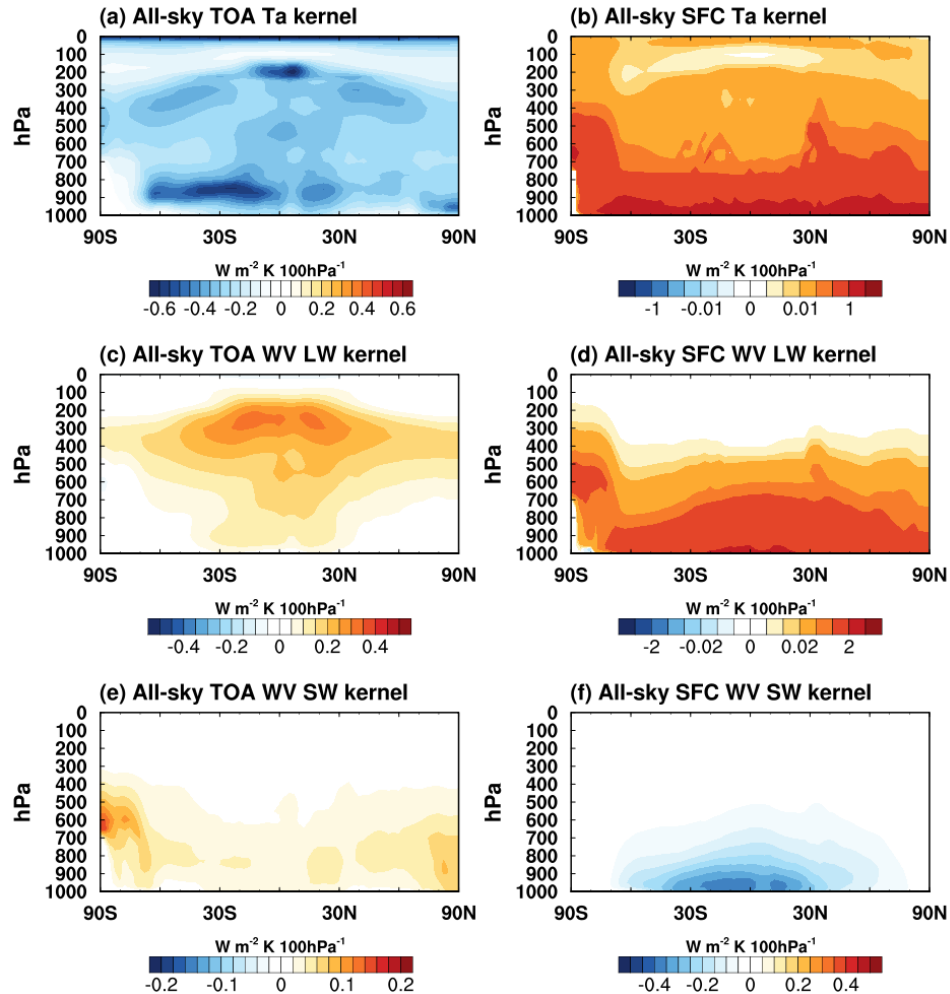
256
257 Figure 2. All-sky (left) TOA and (right) surface ERA5 vertically resolved and zonally
258 averaged kernels of (a, b) air temperature (T_a), (c, d) water vapor longwave ($WV\ LW$) and (e, f)
259 water vapor shortwave ($WV\ SW$), units: W m^{-2} K^{-1} 100hPa^{-1}. Note nonlinear colorbars are used
260 for surface air temperature and water vapor LW kernels and the colorbar ranges differ among
261 panels.

262
263
264 **3.2 Comparison of ERA5 kernels with other datasets**
265
266 To examine the discrepancies between different kernel datasets, we select six previously
267 published ones for comparison. Table 1 summarizes their resolutions and the datasets based on
268 which they are computed, including the GCMs: GFDL (Soden et al., 2008), CAM3 (Shell et al.,
269 2008), CAM5 (Pendergrass et al., 2018), and HadGEM3 (Smith et al., 2020), a global reanalysis:

270 ERAi (Huang et al., 2017), and satellite observations of cloud fields from CloudSat/CALIPSO
271 combined with thermodynamic fields from reanalyses (Kramer et al., 2019b). This list is meant
272 to be representative instead of exhaustive.
273
274   Table 1. Summary of radiative kernels compared in this work. Datasets with * only have
275 TOA kernels.

Radiative kernels	Horizontal resolution (lat*lon)	Vertical levels	Reference
GFDL*	2x2.5	17 (pressure level)	Soden et al., 2008
CAM3*	2.8x2.8	17 (pressure level)	Shell et al., 2008
ERAi	2.5x2.5	24 (pressure level)	Huang et al., 2017
CAM5	0.94x1.25	30 (hybrid level) or 17 (pressure level)	Pendergrass et al., 2018
CloudSat	2x2.5	17 (pressure level)	Kramer et al., 2019b
HadGEM3	1.25x1.9	85 (hybrid level) or 19 (pressure level)	Smith et al., 2020
ERA5	2.5x2.5	37 (pressure level)	This study

276
277
278   To facilitate an intercomparison, these kernel datasets are interpolated to the same
279 horizontal and vertical resolutions as those of the ERA5 kernel when illustrated in Figure 3 and 4
280 (see Figure S5 and S6 for clear-sky) and are uploaded to the same data repository of ERA5
281 kernels. Note that the CAM5 and HadGEM3 kernels have two versions, with one defined at the
282 raw hybrid levels and the other interpolated to pressure levels. To retain the accuracy of them as
283 much as possible, the hybrid level version is used for the interpolation and comparison in Figures
284 3 and 4, while in Section 4, the pressure level version is used for quantifying the feedbacks of
285 CMIP6 models. The GFDL and CAM3 kernels are only available for TOA fluxes and are
286 excluded for surface kernel comparisons.
287   Here we use the standard deviation (std) and its normalized value (std^*) to measure the
288 spread of the inter-kernel dataset differences:

$$std_X = \sqrt{\frac{1}{n-1}\sum_{i=1}^{n}\left(K_X^i - \overline{K_X}\right)^2} \quad (2)$$

289

$$std_X^* = \frac{std_X}{\overline{K_X}} * 100 \quad (3)$$

290

291 where n is the total number of kernel datasets. K_X^i is radiative kernel of variable X from the ith
292 dataset. $\overline{K_X}$ is the multi-dataset mean of radiative kernel K_X. Note that $\overline{K_X}$ does not represent the
293 "truth" value, but a reference value used to measure the spread of multi-kernel values. The
294 vertically integrated and the vertically resolved but zonally averaged distributions of fractional
295 discrepancy (std^*) are shown in Figures 3 and 4, respectively. The zonal mean kernel values
296 from respective multi-datasets are shown in line plots in Figure 3 and 4. Note that some kernels
297 exhibit abnormal values, such as the surface and air temperature kernel of the surface flux in the
298 CAM5 and CloudSat kernels (see Appendix Figure A2), indicating inconsistent computation of
299 their values, and thus are excluded in the corresponding std_X^* statistics in Figures 3 and 4. See
300 more discussions in Appendix.
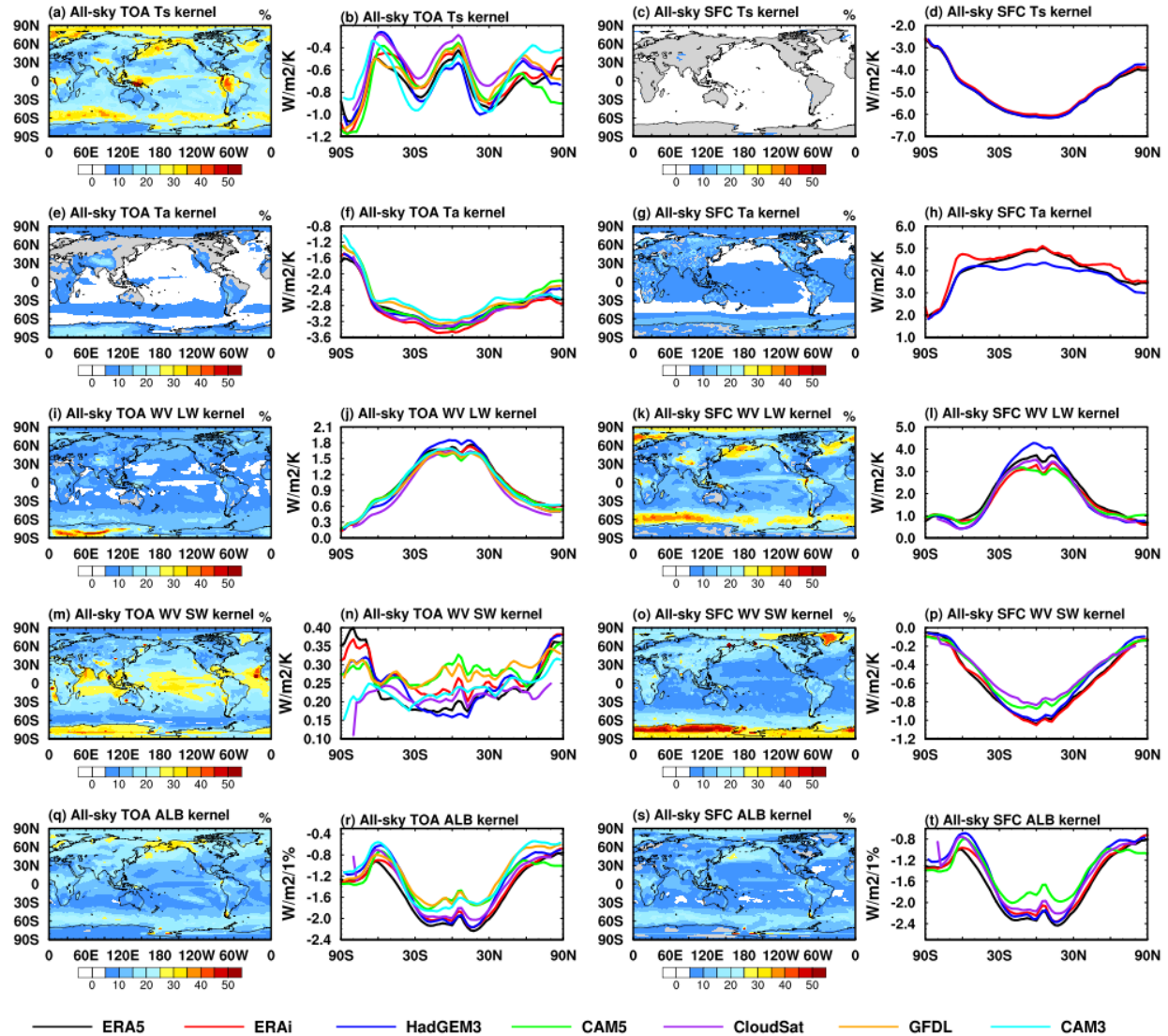
Figure 3. (contour plot) fractional discrepancies as measured by the normalized standard deviation of the kernels by Eq. (3) and (line plot) zonal mean distribution of multi-kernels in all-sky.

The comparisons identify the following relatively larger differences in kernel values. Among the TOA kernels, the surface temperature and albedo kernels show relatively large discrepancies in the Arctic, Southern Ocean and over some continental regions in the tropics in all-sky (Figure 3a and q), with the maximum discrepancy exceeding 30%; the air temperature kernel shows larger discrepancies in the lower troposphere and tropical tropopause region (Figure 4a); these kernel differences are likely due to the differences in cloud fields. The water vapor LW kernel also shows noticeable fractional differences, for example, over the Antarctic region (Figure 3i and 4e). The water vapor SW kernel shows differences in the tropical mid-troposphere and over Antarctic in both clear-sky and all-sky (Figure 4i and S6i), leading to strong variations in the vertical integration of sensitivity (Figure 3m and S5m), with a spread exceeding 30%. The noticeable periodic equatorial pattern in Figure S5m is caused by the CAM3

318   kernel, likely due to a coarser temporal resolution that does not well resolve the diurnal cycle of
319   solar insolation in the kernel computation.
320   For the surface kernels, the most prominent differences exist in SW radiative kernels
321   (Figure 3 and 4), especially in the polar regions. The discrepancy in the water vapor SW kernel
322   reaches 30% for vertically integrated values (Figure 3o), with noticeable differences through the
323   troposphere (Figure 4k). The surface albedo kernel differences are much larger in all-sky than
324   that in clear-sky (Figure 3 and S5), indicating that the cause is in cloud fields, and are also
325   noticeable in the Arctic region due to sea ice variations (Figure 3s). In the LW, the water vapor
326   kernels exhibit noticeable differences in the Central Pacific, Southern Ocean and Arctic in all-
327   sky (Figure 3k), where again the difference in cloud field is likely the cause. The air temperature
328   kernels show noticeable discrepancies in the bottom layers (Figure 4d), which may be caused by
329   inconsistency in the kernel computation and vertical resolutions (see the discussions in
330   Appendix).
331
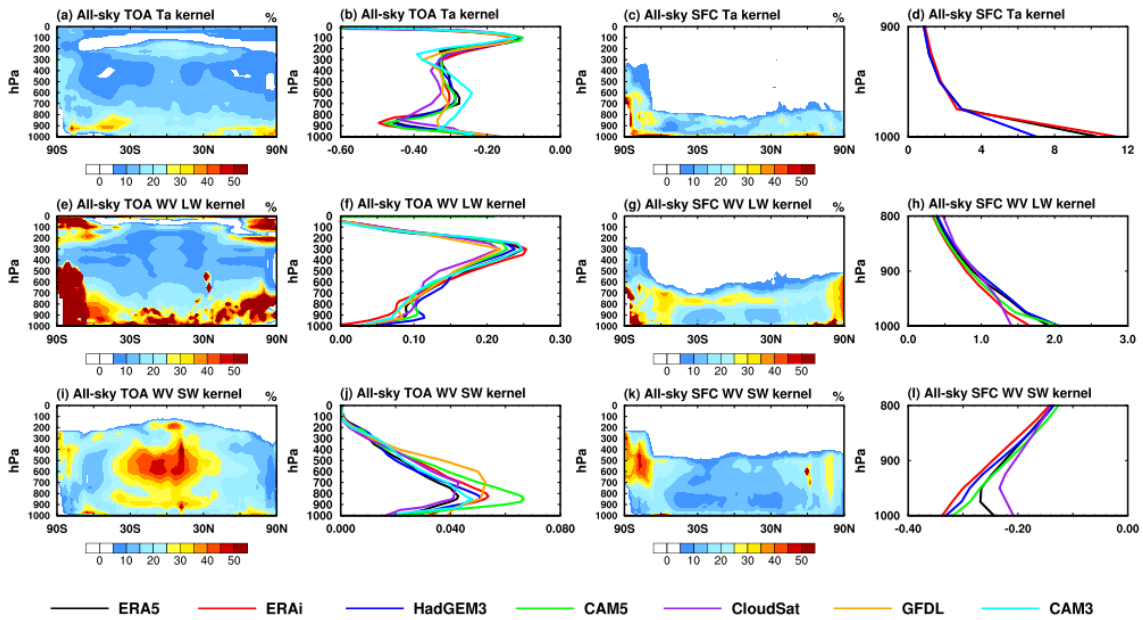
332
333   Figure 4. (contour plot) Cross-section of fraction discrepancies of the radiative kernels, (line
334   plot) global mean vertically resolved kernels from multi-datasets in all-sky.
335
336   In summary, the differences among radiative kernel datasets are generally smaller in clear-
337   sky than in all-sky and in most cases, are mostly within 10% of the radiative kernel values.
338   However, there are some notable regional discrepancies, for example, in the surface temperature
339   kernel in the tropics (Figure 3a), in the surface albedo kernel in the Arctic (Figure 3q), and in the
340   water vapor SW kernel in the Antarctic region (Figure 3m). As different kernel datasets are
341   calculated using different data sources, the discrepancies detected here are likely due to the state-
342   dependency in the kernels, which differ between the kernel datasets. To ascertain the state-
343   dependency-caused kernel uncertainty, we next examine the ERA5 kernels computed from
344   different years, i.e., from different atmospheric states, to investigate how much difference in
345   radiative sensitivity can result from the change in atmospheric state.
346
347

3.3 Interannual variation of kernel values

The intercomparison above identified several prominent inter-dataset differences in the kernel values. For example, there are noticeable differences in the values of surface temperature, albedo and water vapor kernels in the Central Pacific and Arctic region. One possible reason that may account for such differences is the atmospheric state-dependency of the kernel values. Besides the inter-model differences in the different GCM climatology, interannual variations of the atmospheric states, such as cloudiness variations in the Central Pacific region during the ENSO cycle, may affect the radiative sensitivity as some radiative kernels are calculated using one arbitrary year's data. To test this hypothesis, we use the ENSO and sea ice loss cases to demonstrate the changes in radiative sensitivity with a focus on Central Pacific and Arctic region, respectively. In the ENSO case, the variation is defined as the difference in annual mean kernel values between 2015 and 5-year mean (from 2011 to 2015), which have the annual mean sea surface temperature anomalies in the Niño 3.4 region (5N-5S, 190-240E) over +2.0K. In the sea ice loss case, the variation is calculated as the difference in September between year 2012 and 2013, as the sea ice cover in 2012 was reported to be the lowest level in the satellite observation era. In addition, we further show the comparison between ERA5 and ERAi kernels (in Figure 5), which was also calculated by RRTMG and averaged from 5 years' calculations (2008-2012), to compare the inter-kernel difference and interannual difference in kernel values.

To save space, here we only highlight the most prominent differences. Figure 5a-c show the differences in skin temperature, total column water vapor and total cloud cover due to ENSO and Figure 5d-f summarize the corresponding differences in all-sky TOA kernels. As the skin temperature in the Central Pacific warms over 2K (Figure 5a) during ENSO, the increases in water vapor concentration and cloud fraction (Figure 5b and c) reduce the sensitivity of TOA flux to surface temperature change by about 0.2 W m^{-2} K^{-1} (about 33%) (Figure 5d). The moistening in the Central Pacific (Figure 5b) enhances the TOA water vapor LW sensitivity in clear-sky (Figure S7b), while in all-sky the enhanced convection and associated total cloud cover in this region lead to a weakened TOA water vapor LW radiative sensitivity (Figure 5e) despite the moist anomaly, and the decrease is almost contributed from the whole troposphere (Figure S8c). The water vapor SW kernel discrepancy is less pronounced (Figure 5f).

Comparing the 5-year averaged all-sky ERA5 and ERAi kernels, we find that the atmospheric state differences also exist between the atmospheric datasets on which the kernels are computed from. For example, the ERA5 shows similar, but less pronounced, warming anomalies in sea surface temperature in the Central Pacific compared to ERAi, partly due to the strong El Nino year (2015) included in the ERA5 dataset. ERA5 data also shows more water vapor and cloud cover (Figure 5h and i). Although the total column water vapor and total cloud cover are higher in the ERA5 (Figure 5h and i), their differences are complex and vertically non-uniform (Figure S8 d and e), which leads to a slight strengthening of surface temperature kernels compared with ERAi (Figure 5j). It is also noticed that the ERA5 water vapor SW kernel shows lower sensitivity (Figure 5l), which mainly comes from the contributions in mid-to-low troposphere (Figure S8f). The difference noticed in Figure S8 f corresponds to the discrepancy noticed in Figure 4i, which are both in the mid-to-low troposphere, and the corresponding clear-sky kernels are of much less differences (Figure S7), suggesting that the difference in clouds might be the main cause of the all-sky kernel differences, which also correspond to the discrepancies shown in the multi-kernel comparisons in Figure 3a, i, and m.
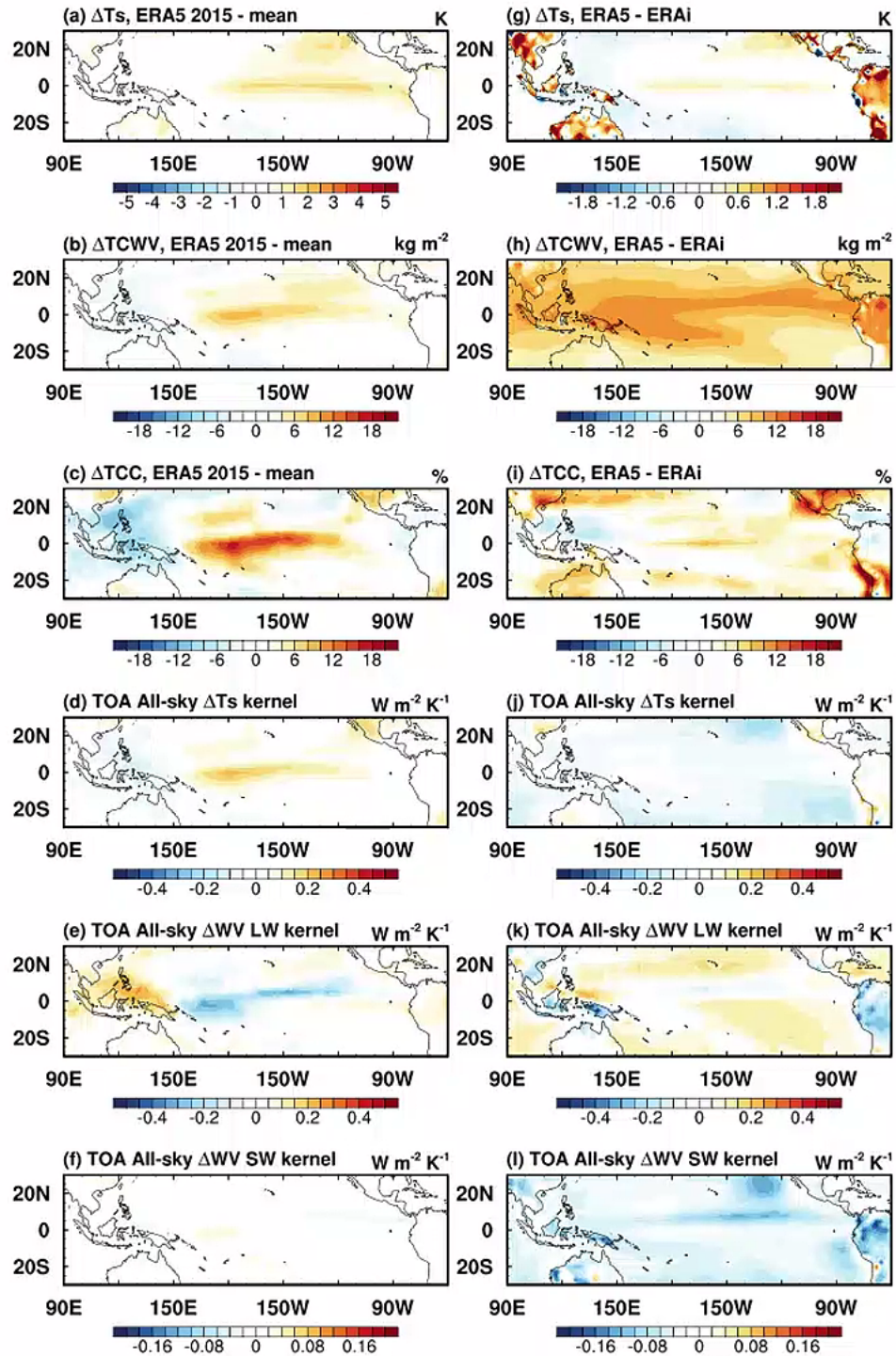
394
395   Figure 5. Differences in climate states and all-sky kernel values (left) between an arbitrary
396   year (2015) and a 5-year mean of ERA5 and (right) between the 5-year means of ERA5 and
397   ERAi datasets: (a, g) skin temperature, (b, h) total column water vapor (TCWV), (c, i) total cloud
398   cover (TCC), (d, j) TOA skin temperature kernel, (e, k) TOA vertically integrated water vapor
399   LW kernel and (f, l) TOA vertically integrated water vapor SW kernel. Note that the colorbar
400   ranges differ among panels.
401
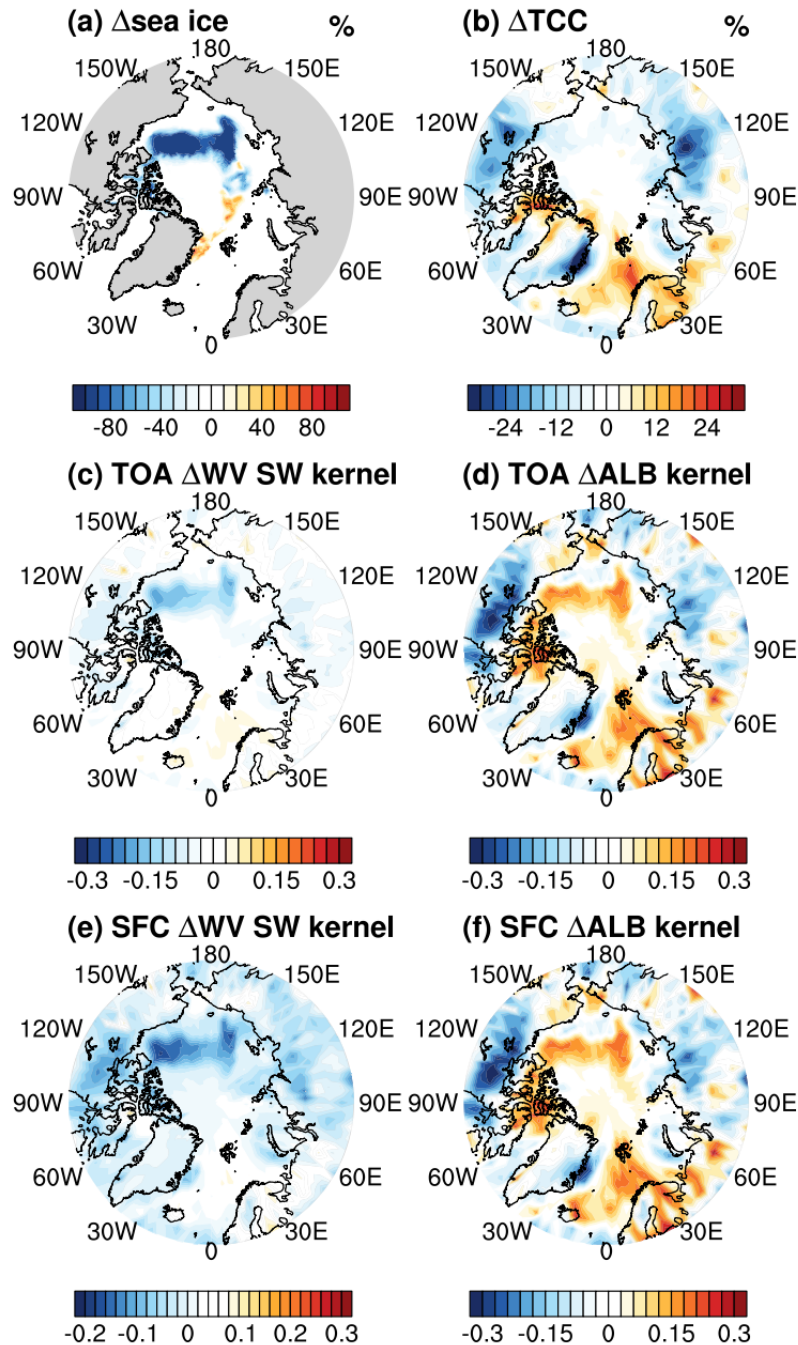
Figure 6. September differences between 2012 and 2013 in (a) sea ice concentration, (b) total cloud cover (TCC), and the differences in (c, e) water vapor SW kernel for TOA and surface fluxes, units: W m^{-2} K^{-1}, (d, f) surface albedo kernel for TOA and surface fluxes, units: W m^{-2} 1%$^{-1}$. Note that the colorbar ranges differ among panels.

In the sea ice loss case, the reduction of sea ice in the Arctic region (Figure 6a) leads to a significant decrease of radiative sensitivity to surface albedo in the areas with noticeable sea ice retreats (Figure 6d and f), with the maximum difference exceeding 30% of the radiative kernel value, because of the nonlinear dependency of the reflected solar radiation on the surface albedo

412 (e.g., see Huang et al., 2021b, Fig. 3 and Fig. 6). The cloud cover changes also contribute to
413 changes in surface albedo kernel values due to the coupling effect between cloud and surface
414 albedo (see Huang et al., 2021b), which for example is seen in the Siberia and to the west
415 coastline of Europe. The change in sea ice also leads to a significant decrease in the TOA
416 sensitivity and an increase of surface sensitivity to water vapor in the sea loss region,
417 respectively (Figure 6c and e), with the maximum changes exceeding 80% for surface. All these
418 results confirm the state-dependency of radiative kernels (e.g., Riihelä et al., 2021).
419   In summary, these quantitatively large interannual differences, as well as their locations,
420 verify that some discrepancies between the radiative kernels are caused by the difference in
421 atmospheric states and partly explain the inter-dataset kernel differences seen in Figure 3 and 4.
422 Nevertheless, it ought to be noted that the differences are localized and because of that do not
423 cause significant differences in the global mean feedback values (see Section 4). The results
424 above also show that kernel values based on one arbitrary year may be regionally different. If
425 only one year's atmospheric profiles are used to generate radiative kernels, we recommend
426 selecting a year without significant anomalies in atmospheric states, e.g., due to El Nino or
427 severe sea ice loss, so that the computed kernel values better represent the radiative sensitivity
428 climatology.
429
430
431 **4. Feedback quantification**
432
433   In this section, we apply different kernels to quantifying the radiative feedbacks in one
434 quadrupling CO_2 experiment (abrupt4xCO_2) of CMIP6 models. This experiment is selected
435 because it has been used by a number of studies for forcing and feedback analyses (e.g., Zelinka
436 et al., 2020), which we can compare our results to. The CMIP6 models used in this assessment
437 are listed in Table2. Note that the standard outputs at 19 pressure levels from the models and
438 correspondingly the kernel values, including CAM5 and HadGEM3, provided at the pressure
439 levels are used in this section.
440
441   Table 2. Summary of CMIP6 models used in this study.

Models	Horizontal resolution (lat*lon)	Vertical levels	Reference
CESM2	0.9*1.25	32 levels to 2.26 hPa	Danabasoglu et al. (2020)
CNRM-CM6-1	1.4*1.4	91 levels to 0.01hPa	Voldoire et al. (2019)
EC-Earth3	0.7*0.7	91 levels to 90 km	Döscher et al. (2022)
HadGEM3-GC31-LL	1.25*1.875	85 levels to 85km	Williams et al. (2018)
IPSL-CM6A-LR	1.3*2.5	79 levels to 80km	Boucher et al. (2020)
MPI-ESM1-2-LR	1.875*1.875	47 levels to 0.01hPa	Mauritsen et al. (2019)

442
443
444 **4.1 Analysis procedure**
445
446 To quantify the radiative feedbacks, data from two experiments as documented by Eyring et al.
447 (2016) and Pincus et al. (2016) are used: abrupt4xCO_2 simulations with an instantaneous

448   quadrupling of CO_2 concentration of year 1850 and piClim-4xCO_2 simulations with SST and sea
449   ice concentrations fixed at the climatology of pre-industrial control experiment and CO_2
450   concentration quadrupled. In each experiment, a 20-year period at the end of the simulation in
451   each model is used. For example, in the models where the abrupt4xCO_2 simulation is longer than
452   150 years, the simulations from the last 20 years rather than those from years 131 to 150 are used
453   for the calculation. To exclude the effect of rapid adjustments, the radiative feedbacks in this
454   study are measured using the difference of feedback variables between the abrupt4xCO_2 and
455   piClim-4xCO_2 experiments and vertically integrated from the surface to model top. Note that
456   these treatments are different from some other studies, e.g., Zelinka et al., 2020, which used
457   piControl simulation as the climatology baseline and vertical integration from the surface to the
458   tropopause, although the quantitative differences in the diagnosed global mean feedback values
459   are small.
460   To detail the analysis procedure, firstly, all variables including radiative fluxes and
461   atmospheric variables from CMIP6 models are interpolated to the horizontal and vertical
462   resolution of the kernel itself. Note that for CAM3, GFDL, CloudSat and CAM5 kernels, they
463   only have 17 pressure levels which are two layers (1hPa and 5hPa) fewer than the CMIP6
464   standard model output. To address this issue, the contribution of the two missing layers is
465   calculated using other kernels (e.g., ERA5) and found to have negligible effect on the global
466   mean feedback value. Hence, when using these three kernels, the contributions from 10hPa
467   above are ignored.
468   Secondly, the non-cloud radiative feedback of variable X (ΔR_X) is calculated as:
469         $\Delta R_X = K_X \cdot \Delta X$ (4)
470   with units in W m^{-2}, where K_X is the monthly mean radiative kernel of variable X and ΔX is the
471   monthly mean anomaly of X measured by the difference between abrupt4xCO_2 and piClim-
472   4xCO_2, and represents the anomalies of surface temperature (ΔT_s), air temperature (ΔT_a), water
473   vapor (ΔWV) and surface albedo (ΔALB). For the 2D radiative kernels (surface temperature and
474   surface albedo), K_X and ΔX have just single layer values and ΔR_X is simply the product of these
475   two terms. For the 3D radiative kernels (air temperature and water vapor), both K_X and ΔX are
476   vectors of pressure levels and ΔR_X is the dot product of K_X and ΔX and is integrated from the
477   TOA to 1000hPa. Note that if K_X is normalized with unit pressure thickness (e.g., W m^{-2} K^{-1}
478   100hPa^{-1}), the layer thickness must be taken into account when calculating dR_X. See Appendix
479   for further discussion on the application of thickness-weighted kernels.
480   Finally, cloud feedbacks are diagnosed using the adjusted cloud-radiative forcing method
481   (Shell et al., 2008). Here we compute the residual term in clear-sky as:
482         $res^o = \Delta R^o - \sum \Delta R_X^o$ (5)
483   which represents the unexplained part of radiation budget change, and assuming the all-sky
484   decomposition has the same non-closure residual, the cloud feedback, is measured as
485         $\Delta R_C = \Delta R - \sum \Delta R_X - res^o$ (6)
486   where the superscript o represents clear-sky quantities. $\sum \Delta R_X^o$ and $\sum \Delta R_X$ are the sum of non-
487   cloud feedbacks in clear-sky and all-sky, respectively, diagnosed by multiplying the radiative
488   kernel with the atmospheric responses measured as the difference between abrupt4xCO_2 and
489   piClim-4xCO_2 experiments. ΔR^o and ΔR are the total radiation change in clear-sky and all-sky,
490   respectively, calculated as the difference in the GCM-simulated radiative fluxes between two
491   experiments. It is worth noting that ΔR_C measured according to Eq. (6) is essentially the part of
492   total radiation change not explained by the non-cloud feedbacks and is equivalent to the other
493   formulations of the adjusted cloud radiative effect method (e.g., Soden et al., 2008; Huang,

494 2013). Interested readers can refer to, for example, Huang (2013) for a detailed formulation and
495 explanations of the method.
496   The feedback parameters, λ_X, in the units of W m^{-2} K^{-1}, are then obtained by normalizing
497 the feedback flux changes ΔR_X by the global mean surface temperature change ΔT_S in the
498 abrupt4xCO$_2$ experiment:
499      $\lambda_X = \Delta R_X / \Delta T_S$ \hfill (7)
500
501
502 **4.2 TOA feedbacks**
503
504   The residual term (res^o) measures the unexplained radiation change in the feedback
505 analysis and provides a useful overall indication of the soundness of the feedback quantification.
506 Figure 7 illustrates the residual term for the TOA flux decomposition when different kernels are
507 used to diagnose the multi-model mean feedbacks. In terms of the global mean, all residual terms
508 are of small magnitude, no matter which kernel dataset is used (Figure 8 and Table S1).
509 However, there are some noticeable local residuals, especially for the SW budget, e.g., in the
510 Arctic region and around the Antarctic continent where sea ice changes the most (mid-column in
511 Figure 7). While the non-zero magnitude of the residual is partly due to nonlinearity in the
512 radiation decomposition, e.g., possible coupling between surface albedo and water vapor (Huang,
513 Y. et al., 2021), the spread among the kernel results as evidenced by the line plots of Figure 7 is
514 attributable to the discrepancies in the SW radiative kernels as revealed by the comparisons in
515 Section 3. In the LW, the residual is generally small compared with the total feedback. In
516 summary, the residual terms for the TOA budget are small in terms of the global mean feedback
517 strengths, affirming the validity of the radiative kernels for feedback quantification. Here, we use
518 the spatial root-mean square (RMS) of the residuals to quantify the regional biases, which are
519 shown by the numbers on the right corner of each panel in Figure 7. For LW, results from ERA5,
520 ERAi and CAM5 kernels show relatively smaller regional biases compared to those from
521 HadGM3, CloudSat and CAM3 kernels. For SW, all kernel datasets have similar regional non-
522 closures, for example, in the Polar regions (Figure 7 and 8). This is largely caused by the non-
523 linearity in albedo feedback and also the coupling effect between water vapor and surface albedo
524 feedbacks (Huang et al., 2021b; Block and Mauritsen, 2013). In summary, these results suggest
525 that for the TOA feedback quantification, the performance of ERA5 kernel is comparable to the
526 other datasets.
527   Figure 8 compares the spreads of feedback values resulted from the differences in kernels
528 and those from the different projections of GCMs. In general, feedbacks from different kernel
529 datasets overlap each other, even for cloud feedbacks, indicating a good consistency between the
530 results computed from different kernel datasets. However, the spread across the GCMs is
531 considerably larger, suggesting the overall feedback uncertainty is dominated by inter-model
532 spread rather than the kernel uncertainty. The values of the feedbacks from each model and
533 kernel datasets are shown in Table S1 and S2 for readers who are interested. These results are
534 consistent with other published results. For example, compared with the results of Zelinka et al.
535 (2020) based on the ERAi kernel, the kernel-diagnosed overall feedback parameter in the two
536 results is -0.87 W m^{-2} K^{-1} and -0.85 W m^{-2} K^{-1} for the CNRM-CM6-1 model and -0.81 W m^{-2} K^{-1}
537 and -0.84 W m^{-2} K^{-1} for the HadGEM3-GC3-LL model.
538   In summary, in terms of TOA feedback values, the inter-kernel differences lead to small
539 uncertainty in the analyzed non-cloud feedbacks; the kernel-induced uncertainty in cloud

540 feedback is relatively larger (Table S2), with the inter-kernel spread in cloud LW feedback
541 almost equally from the spread in surface and air temperature feedback and water vapor LW
542 feedback (as measured by the $\sum \Delta R_X^o - \sum \Delta R_X$ terms in Eq. (6)), and the inter-kernel spread in
543 cloud SW feedback more from the spread in surface albedo feedback than from water vapor SW
544 feedback (not shown); despite this, this uncertainty is considerably less than the inter-GCM
545 cloud feedback spread.
546
547
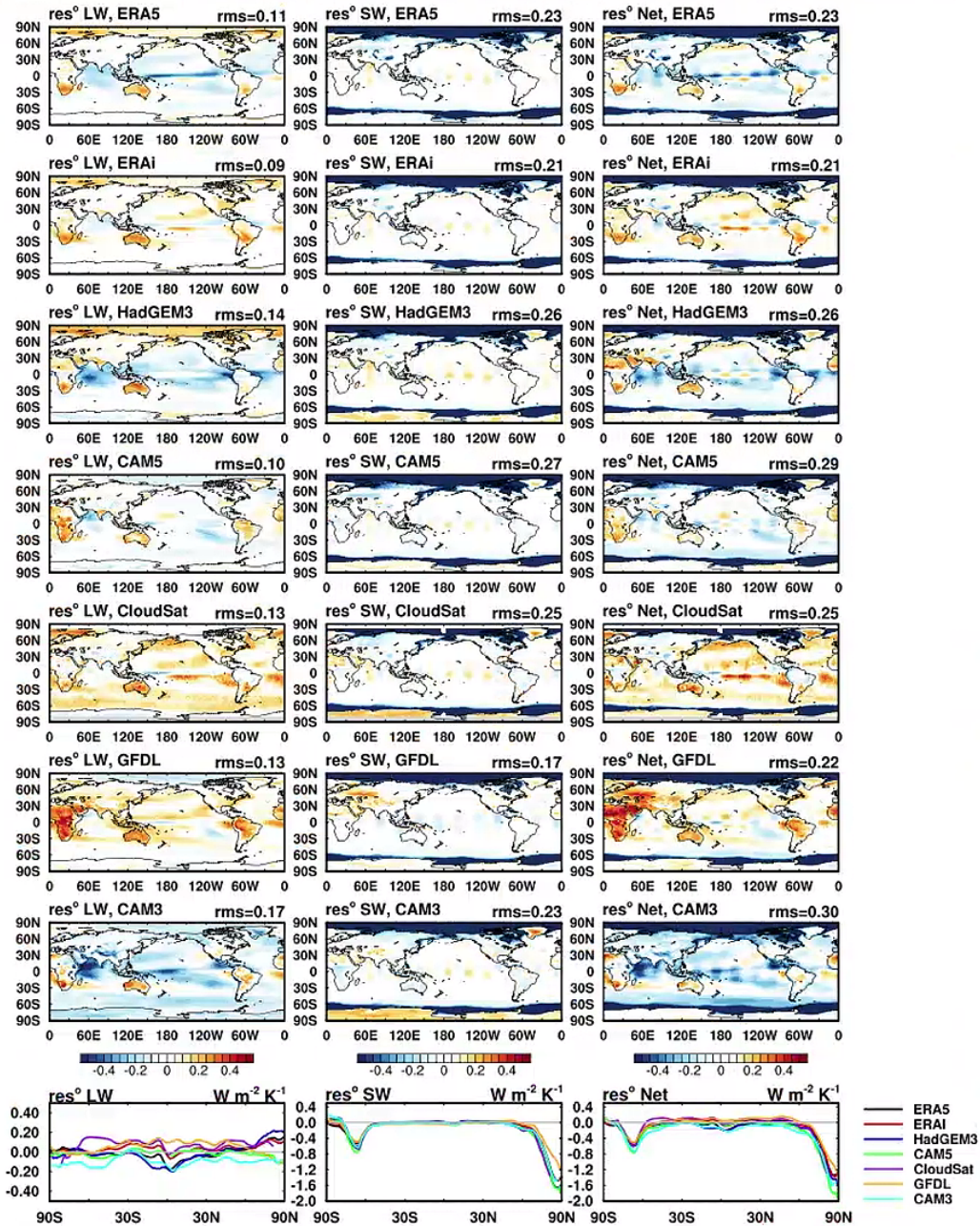
548
549 Figure 7. The residuals (res^o) in the multi-model mean TOA feedback decomposition
550 when different kernels are used, (left column) LW, (mid-column) SW, (right-column) Net, the

551 sum of LW and SW. The three line-plots in the bottom row are the zonal mean residuals.
552 Numbers on the right corner in each panel are the spatial root-mean-square values.
553
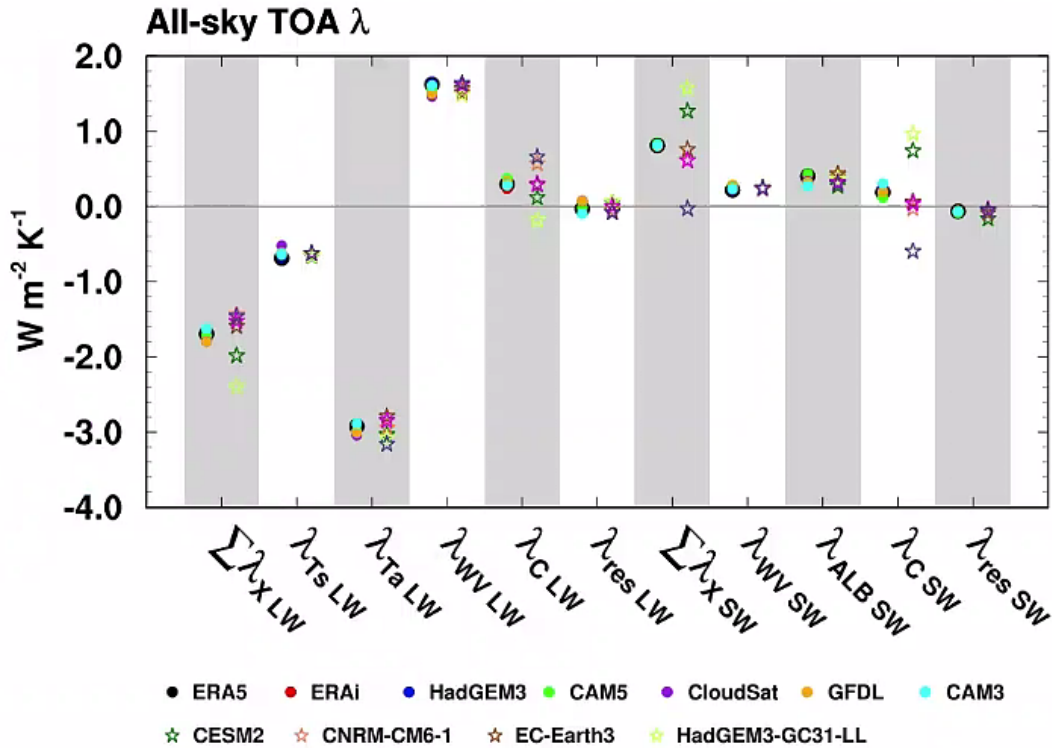
554
555 Figure 8. Global mean TOA feedback parameters in all-sky diagnosed by the kernels listed in
556 Table 1 across CMIP6 models. Dot marks represent multi-model mean values computed from
557 different kernel datasets. Stars represent the multi-kernel mean results computed from different
558 GCMs.
559
560
561 **4.3 Surface feedbacks**
562
563   Next, we examine how the inter-kernel differences lead to uncertainty in the analyzed
564 surface feedbacks.
565   Figure 9 shows the residual distribution. We find that when the ERA5 and ERAi kernels
566 are used for the feedback analysis, the non-closure residual in the surface budget is comparable
567 in magnitude to the TOA analysis. This suggests that the surface kernels afford a valid tool for
568 the surface feedback analysis. However, some prominent biases are noticed for other kernel
569 datasets. For example, the HadGEM3 kernels, show especially an underestimation in air
570 temperature feedback, likely due to a biased sensitivity of the bottom atmospheric layer (see
571 Appendix for more discussions). The sum of global mean surface and air temperature feedback
572 parameter measured by the HadGEM3 kernel is around -3.70 W m^{-2} K^{-1} (Table S4, compared to
573 around -1.0 W m^{-2} K^{-1} measured by the other kernels), and the non-closure residual is as large as
574 3.0 W m^{-2} K^{-1} (Table S3, compared to -0.1 W m^{-2} K^{-1} in the others). For this reason, the result
575 from HadGEM3 kernel is excluded for the multi-kernel statistics in Figure 10, Table S3 and S4,
576 but listed in a separate row for comparison. From either the spatial distribution of residual term

577 or the spatial RMS residuals, the ERA5 kernel and ERAi kernel show a superior performance
578 than other datasets. The use of ERA5 kernels may be advantageous for diagnosing the surface
579 radiation budget, considering that ERA5 data is a newer version reanalysis dataset from ECMWF
580 compared with ERAi and its data quality has been widely validated.
581   Figure 10 compares the inter-model and inter-kernel spreads for the surface feedbacks.
582 Unlike the results for TOA, the inter-kernel spread can be as large as the inter-model spread, for
583 example, in LW surface temperature feedback, air temperature feedback and water vapor
584 feedback. The sum of air temperature and surface temperature feedbacks shows better
585 consistency compared with the respective components (except for the HadGEM3 kernel), and the
586 respective air temperature and surface temperature feedbacks quantified by the ERA5 kernel are
587 stronger than the results from the other kernels. These discrepancies are due to the reason
588 discussed in the Appendix – a possibly wrong quantification of surface temperature effect. In
589 SW, the multi-kernel results are close to each other, showing smaller inter-kernel spreads than
590 the inter-model spreads.
591   In summary, we find the surface feedback decomposition can achieve similar level of
592 radiation closure to the TOA analysis when using ERA5 kernels, affirming the validity of kernels
593 for diagnosing the surface radiative feedback. However, the results qualitatively vary depending
594 on which kernel dataset is used, indicating errors in the computation of some kernels.
595
596
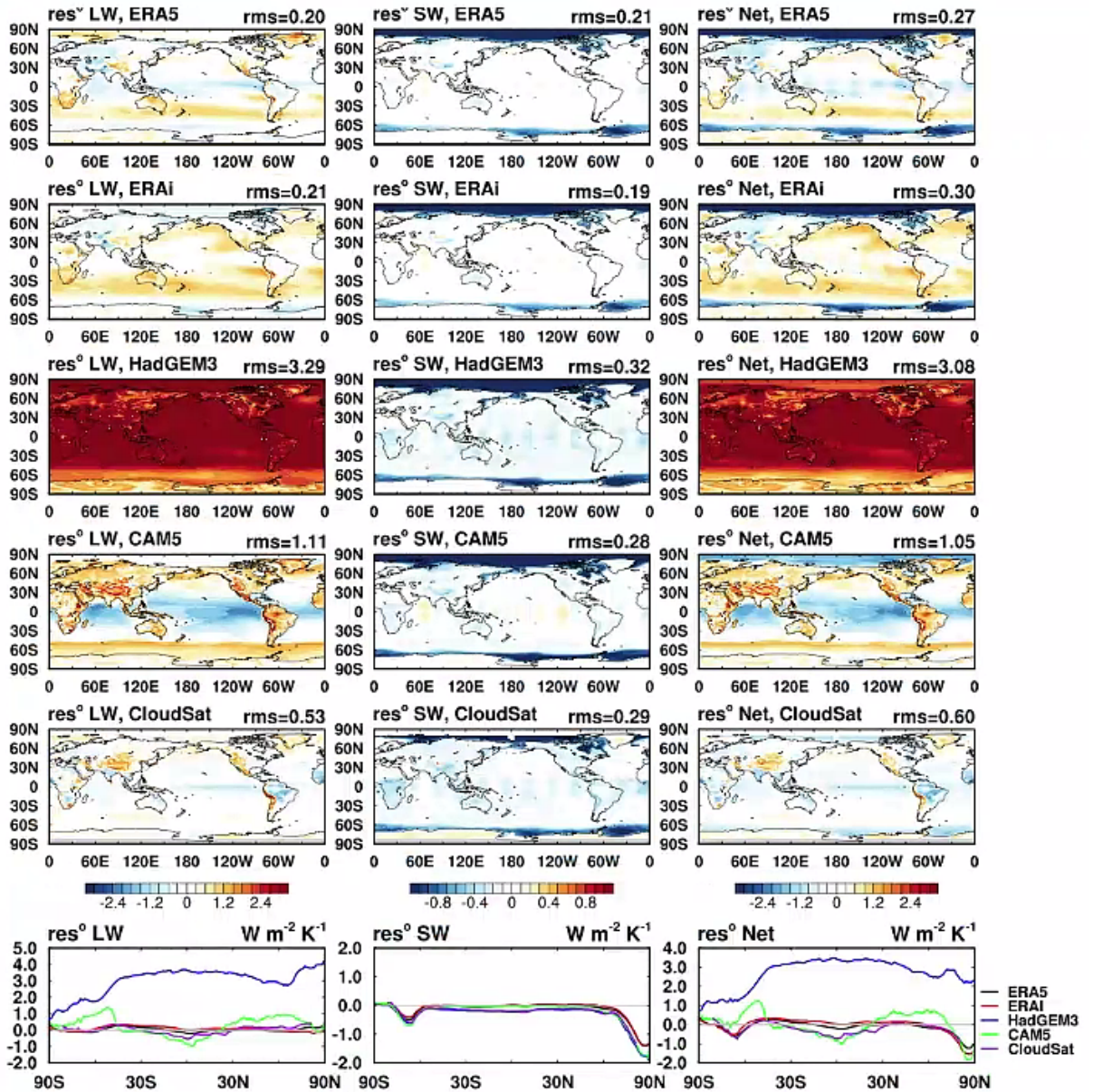
597
598   Figure 9. Similar to Figure 7, but for the surface feedback analysis.
599
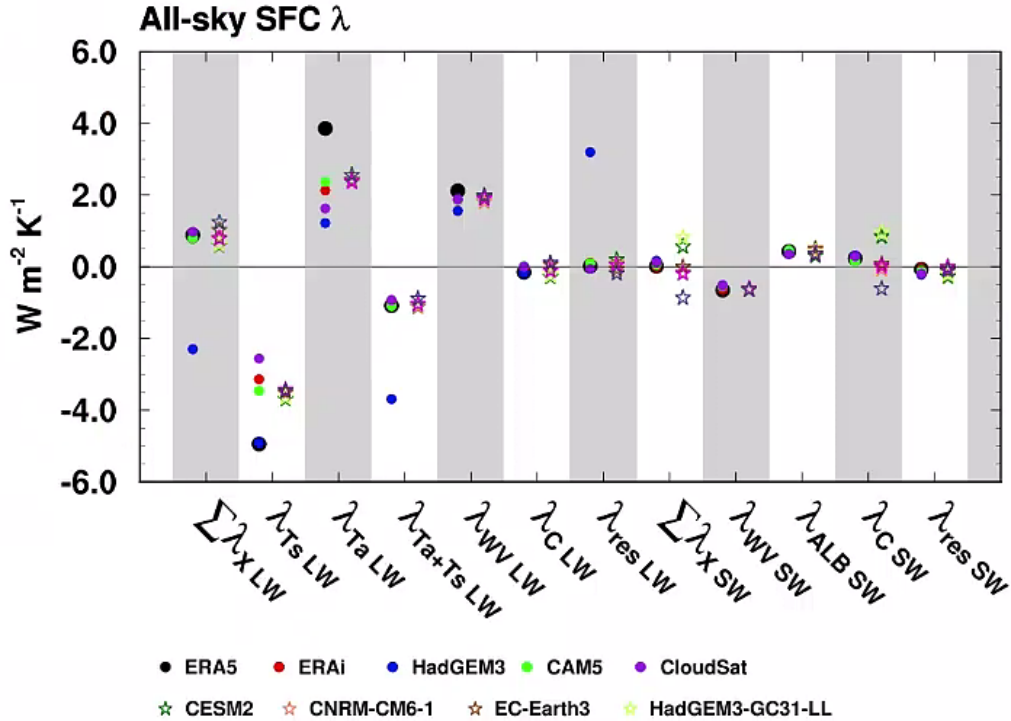
Figure 10. Similar to Figure 8, but for the surface feedback parameter.

5. Data availability

The datasets containing the multi-year averaged monthly mean TOA and surface kernels for surface temperature, air temperature, surface albedo and water vapor (LW and SW) are available at: http://dx.doi.org/10.17632/vmg3s67568.3 (Huang and Huang, 2023). Other kernel datasets used in this study, interpolated to the same horizontal and vertical grids of the ERA5 kernels, are also provided at this link.

6. Conclusions and discussions

In this paper, we present a newly generated set of ERA5-based radiative kernels of surface and air temperatures, water vapor and surface albedo, for both TOA and surface radiation fluxes. We also compare them with other published kernels, including the kernel-diagnosed radiative feedbacks for both the TOA and surface radiation budgets.

For the TOA kernels, the results here demonstrate general consistency among the different kernel datasets, and the discrepancies are generally within 10% in terms of vertically integrated or globally averaged radiative sensitivity, although some relatively larger regional differences are noticed, including those in the surface temperature kernel in the tropics (Figure 3a), those in the surface albedo kernel in the Arctic (Figure 3q) and those in the water vapor shortwave kernel over Antarctica (Figure 3m), which is partly due to the dependence of radiative sensitivity on background climate states.

For the surface kernels, more prominent inter-kernel differences are found. For example, the differences in the water vapor shortwave kernel in the Antarctic (Figure 3o) and in the

surface albedo kernel in the Arctic (Figure 3s) can reach 30% of the kernel value itself. Some kernels have considerably biased air temperature sensitivity values in the bottom atmospheric layers, which is likely due to improper treatment in the perturbation experiments used for kernel computation (see Appendix). The differences in both TOA and surface kernels discovered here emphasize the importance of validating the radiative sensitivity as noted by Huang and Wang (2019) and Pincus et al. (2020).

The investigation of interannual variability in ERA5 kernels validates the dependence of radiative sensitivity on atmospheric state and the further comparison between ERAi and ERA5 kernel (Figure 5) reveals the effects of clouds on the kernel values, which might explain the discrepancies of multi-kernel datasets (Figure 3).

Applying the different kernels to quantifying the TOA and surface radiative feedbacks, we find that for TOA feedback quantification, the ERA5 kernels are as accurate as other kernel datasets, while for surface feedback, ERA5 and ERAi kernels show superior accuracy compared with other datasets. Considering the strengths of the ERA5 dataset in representing the atmospheric states, we recommend the use of ERA5 kernels.

In addition, we compare the feedback differences caused by using different kernels and also the inter-GCM spread of the feedback values (when measured by the same kernel). We find the kernel difference is not a major cause of the inter-GCM TOA feedback spread (Figure 7 and 8). This finding is consistent with the previous assessments (e.g., Soden et al., 2008; Jonko et al., 2012; Vial et al. 2013).

Radiation closure tests show that the unexplained residuals are generally within 10% of the total feedback for both TOA and surface analyses in terms of the global mean feedback, confirming the validity of the kernels for feedback quantification for both budgets. This suggests that the large non-closure residuals reported in some previous studies (e.g., Vargas Zeppetello, et al., 2019) are likely due to kernel inaccuracy rather than the limitation of the kernel method. However, there are more significant local non-closures, for example, in the shortwave in the Arctic region and around the Antarctic continent, which is contributed, but cannot be fully explained, by the kernel uncertainty. This points to the accuracy limit of the kernel (linear) method and calls for more advanced methods, such as the neural network method (Zhu et al., 2019), for local feedback analysis.

Author contributions

HH and YH led the design of this research and the writing of the manuscript. HH produced the ERA5 radiative kernel and provided calculations of the inter-kernel comparison and feedback analysis.

Competing interests
The authors declare that they have no conflict of interest.

Acknowledgements

We thank Mark Zelinka, Ryan Kramer and one anonymous reviewer for their helpful reviews. We acknowledge the grants from the Natural Sciences and Engineering Research Council of Canada (RGPIN-2019-04511) and the Fonds de Recherché Nature et Technologies of

673 Quebec (2021-PR-283823) that supported this research. H. Huang thanks Yonggang Liu, Jun
674 Yang and Qiang Wei for hosting her visit at Peking University, during which time part of this
675 work was completed.

676
677

References

679 Block, K. and Mauritsen, T.: Forcing and feedback in the MPI‑ESM‑LR coupled model under
680   abruptly quadrupled CO2, Journal of Advances in Modeling Earth Systems, 5, 676-691, 2013.
681 Boucher, O., Servonnat, J., Albright, A. L., Aumont, O., Balkanski, Y., Bastrikov, V., Bekki, S.,
682   Bonnet, R., Bony, S., and Bopp, L.: Presentation and evaluation of the IPSL‑CM6A‑LR
683   climate model, Journal of Advances in Modeling Earth Systems, 12, e2019MS002010, 2020.
684 Bright, R. M. and O'Halloran, T. L.: Developing a monthly radiative kernel for surface albedo<?
685   xmltex\break?> change from satellite climatologies of Earth's shortwave<? xmltex\break?>
686   radiation budget: CACK v1. 0, Geoscientific Model Development, 12, 3975-3990, 2019.
687 Chao, L.-W. and Dessler, A. E.: An assessment of climate feedbacks in observations and climate
688   models using different energy balance frameworks, Journal of Climate, 34, 9763-9773, 2021.
689 Collins, W., Ramaswamy, V., Schwarzkopf, M. D., Sun, Y., Portmann, R. W., Fu, Q., Casanova, S.,
690   Dufresne, J. L., Fillmore, D. W., and Forster, P.: Radiative forcing by well‑mixed
691   greenhouse gases: Estimates from climate models in the Intergovernmental Panel on Climate
692   Change (IPCC) Fourth Assessment Report (AR4), Journal of Geophysical Research:
693   Atmospheres, 111, 2006.
694 Colman, R. and McAvaney, B.: A study of general circulation model climate feedbacks determined
695   from perturbed sea surface temperature experiments, Journal of Geophysical Research:
696   Atmospheres, 102, 19383-19402, 1997.
697 Danabasoglu, G., Lamarque, J. F., Bacmeister, J., Bailey, D., DuVivier, A., Edwards, J., Emmons,
698   L., Fasullo, J., Garcia, R., and Gettelman, A.: The community earth system model version 2
699   (CESM2), Journal of Advances in Modeling Earth Systems, 12, e2019MS001916, 2020.
700 Dessler, A. E.: A determination of the cloud feedback from climate variations over the past decade,
701   Science, 330, 1523-1527, 2010.
702 Doelling, D. R., Loeb, N. G., Keyes, D. F., Nordeen, M. L., Morstad, D., Nguyen, C., Wielicki, B.
703   A., Young, D. F., and Sun, M.: Geostationary enhanced temporal interpolation for CERES
704   flux products, Journal of Atmospheric and Oceanic Technology, 30, 1072-1090, 2013.
705 Dong, Y., Armour, K. C., Zelinka, M. D., Proistosescu, C., Battisti, D. S., Zhou, C., and Andrews,
706   T.: Intermodel spread in the pattern effect and its contribution to climate sensitivity in CMIP5
707   and CMIP6 models, Journal of Climate, 33, 7755-7775, 2020.
708 Donohoe, A., Blanchard-Wrigglesworth, E., Schweiger, A., and Rasch, P. J.: The effect of
709   atmospheric transmissivity on model and observational estimates of the sea ice albedo
710   feedback, Journal of Climate, 33, 5743-5765, 2020.
711 Döscher, R., Acosta, M., Alessandri, A., Anthoni, P., Arsouze, T., Bergman, T., Bernardello, R.,
712   Boussetta, S., Caron, L.-P., and Carver, G.: The EC-Earth3 Earth system model for the
713   Coupled Model Intercomparison Project 6, Geoscientific Model Development, 15, 2973-3020,
714   2022.
715 Eyring, V., Bony, S., Meehl, G. A., Senior, C. A., Stevens, B., Stouffer, R. J., and Taylor, K. E.:
716   Overview of the Coupled Model Intercomparison Project Phase 6 (CMIP6) experimental
717   design and organization, Geoscientific Model Development, 9, 1937-1958, 2016.
718 Graham, R. M., Hudson, S. R., and Maturilli, M.: Improved performance of ERA5 in Arctic

gateway relative to four global atmospheric reanalyses, Geophysical Research Letters, 46, 6138-6147, 2019.

Hersbach, H., Bell, B., Berrisford, P., Hirahara, S., Horányi, A., Muñoz‑Sabater, J., Nicolas, J., Peubey, C., Radu, R., and Schepers, D.: The ERA5 global reanalysis, Quarterly Journal of the Royal Meteorological Society, 146, 1999-2049, 2020.

Huang, H. and Huang, Y.: Nonlinear coupling between longwave radiative climate feedbacks, Journal of Geophysical Research: Atmospheres, 126, e2020JD033995, 2021.

Huang, H., Huang, Y., and Hu, Y.: Quantifying the energetic feedbacks in ENSO, Climate Dynamics, 56, 139-153, 2021.

Huang, Y.: On the longwave climate feedbacks, Journal of climate, 26, 7603-7610, 2013.

Huang, Y. and Wang, Y.: How does radiation code accuracy matter?, Journal of Geophysical Research: Atmospheres, 124, 10742-10752, 2019.

Huang, Y., Huang, H., and Shakirova, A.: The nonlinear radiative feedback effects in the Arctic warming, Frontiers in Earth Science, 651, 2021.

Huang, Y., Ramaswamy, V., and Soden, B.: An investigation of the sensitivity of the clear‑sky outgoing longwave radiation to atmospheric temperature and water vapor, Journal of Geophysical Research: Atmospheres, 112, 2007.

Huang, Y., Xia, Y., and Tan, X.: On the pattern of CO_2 radiative forcing and poleward energy transport, Journal of Geophysical Research: Atmospheres, 122, 10,578-510,593, 2017.

Huang, Y., Chou, G., Xie, Y., and Soulard, N.: Radiative control of the interannual variability of Arctic sea ice, Geophysical Research Letters, 46, 9899-9908, 2019.

Jonko, A. K., Shell, K. M., Sanderson, B. M., and Danabasoglu, G.: Climate feedbacks in CCSM3 under changing CO_2 forcing. Part I: Adapting the linear radiative kernel technique to feedback calculations for a broad range of forcings, Journal of Climate, 25, 5260-5272, 2012.

Kolly, A. and Huang, Y.: The radiative feedback during the ENSO cycle: Observations versus models, Journal of Geophysical Research: Atmospheres, 123, 9097-9108, 2018.

Kramer, R. J., Soden, B. J., and Pendergrass, A. G.: Evaluating Climate Model Simulations of the Radiative Forcing and Radiative Response at Earth's Surface, Journal of Climate, 32, 4089-4102, 2019a.

Kramer, R. J., Matus, A. V., Soden, B. J., and L'Ecuyer, T. S.: Observation‑based radiative kernels from CloudSat/CALIPSO, Journal of Geophysical Research: Atmospheres, 124, 5431-5444, 2019b.

Mauritsen, T., Bader, J., Becker, T., Behrens, J., Bittner, M., Brokopf, R., Brovkin, V., Claussen, M., Crueger, T., and Esch, M.: Developments in the MPI‑M Earth System Model version 1.2 (MPI‑ESM1. 2) and its response to increasing CO_2, Journal of Advances in Modeling Earth Systems, 11, 998-1038, 2019.

Mlawer, E. J., Taubman, S. J., Brown, P. D., Iacono, M. J., and Clough, S. A.: Radiative transfer for inhomogeneous atmospheres: RRTM, a validated correlated‑k model for the longwave, Journal of Geophysical Research: Atmospheres, 102, 16663-16682, 1997.

Myhre, G., Kramer, R., Smith, C., Hodnebrog, Ø., Forster, P., Soden, B., Samset, B., Stjern, C., Andrews, T., and Boucher, O.: Quantifying the importance of rapid adjustments for global precipitation changes, Geophysical Research Letters, 45, 11,399-311,405, 2018.

Pendergrass, A. G. and Hartmann, D. L.: The atmospheric energy constraint on global-mean precipitation change, Journal of climate, 27, 757-768, 2014.

Pendergrass, A. G., Conley, A., and Vitt, F. M.: Surface and top-of-atmosphere radiative feedback kernels for CESM-CAM5, Earth System Science Data, 10, 317-324, 2018.

Pincus, R., Buehler, S. A., Brath, M., Crevoisier, C., Jamil, O., Franklin Evans, K., Manners, J., Menzel, R. L., Mlawer, E. J., and Paynter, D.: Benchmark calculations of radiative forcing by greenhouse gases, Journal of Geophysical Research: Atmospheres, 125, e2020JD033483, 2020.

Previdi, M.: Radiative feedbacks on global precipitation, Environmental Research Letters, 5, 025211, 2010.

Riihelä, A., Bright, R. M., and Anttila, K.: Recent strengthening of snow and ice albedo feedback driven by Antarctic sea-ice loss, Nature Geoscience, 14, 832-836, 2021.

Shell, K. M., Kiehl, J. T., and Shields, C. A.: Using the radiative kernel technique to calculate climate feedbacks in NCAR's Community Atmospheric Model, Journal of Climate, 21, 2269-2282, 2008.

Smith, C. J., Kramer, R. J., and Sima, A.: The HadGEM3-GA7. 1 radiative kernel: the importance of a well-resolved stratosphere, Earth System Science Data, 12, 2157-2168, 2020.

Soden, B. J. and Held, I. M.: An assessment of climate feedbacks in coupled ocean–atmosphere models, Journal of climate, 19, 3354-3360, 2006.

Soden, B. J., Held, I. M., Colman, R., Shell, K. M., Kiehl, J. T., and Shields, C. A.: Quantifying climate feedbacks using radiative kernels, Journal of Climate, 21, 3504-3520, 2008.

Taylor, K. E., Stouffer, R. J., and Meehl, G. A.: An overview of CMIP5 and the experiment design, Bulletin of the American meteorological Society, 93, 485-498, 2012.

Thorsen, T. J., Kato, S., Loeb, N. G., and Rose, F. G.: Observation-based decomposition of radiative perturbations and radiative kernels, Journal of climate, 31, 10039-10058, 2018.

Vargas Zeppetello, L., Donohoe, A., and Battisti, D.: Does surface temperature respond to or determine downwelling longwave radiation?, Geophysical Research Letters, 46, 2781-2789, 2019.

Vial, J., Dufresne, J.-L., and Bony, S.: On the interpretation of inter-model spread in CMIP5 climate sensitivity estimates, Climate Dynamics, 41, 3339-3362, 2013.

Voldoire, A., Saint‐Martin, D., Sénési, S., Decharme, B., Alias, A., Chevallier, M., Colin, J., Guérémy, J. F., Michou, M., and Moine, M. P.: Evaluation of CMIP6 deck experiments with CNRM‐CM6‐1, Journal of Advances in Modeling Earth Systems, 11, 2177-2213, 2019.

Wetherald, R. and Manabe, S.: Cloud feedback processes in a general circulation model, Journal of the Atmospheric Sciences, 45, 1397-1416, 1988.

Williams, K., Copsey, D., Blockley, E., Bodas‐Salcedo, A., Calvert, D., Comer, R., Davis, P., Graham, T., Hewitt, H., and Hill, R.: The Met Office global coupled model 3.0 and 3.1 (GC3. 0 and GC3. 1) configurations, Journal of Advances in Modeling Earth Systems, 10, 357-380, 2018.

Wright, J. S., Sun, X., Konopka, P., Krüger, K., Legras, B., Molod, A. M., Tegtmeier, S., Zhang, G. J., and Zhao, X.: Differences in tropical high clouds among reanalyses: origins and radiative impacts, Atmospheric Chemistry and Physics, 20, 8989-9030, 2020.

Yue, Q., Kahn, B. H., Fetzer, E. J., Schreier, M., Wong, S., Chen, X., and Huang, X.: Observation-based longwave cloud radiative kernels derived from the A-Train, Journal of Climate, 29, 2023-2040, 2016.

Zelinka, M. D., Klein, S. A., and Hartmann, D. L.: Computing and partitioning cloud feedbacks using cloud property histograms. Part I: Cloud radiative kernels, Journal of Climate, 25, 3715-3735, 2012.

Zelinka, M. D., Myers, T. A., McCoy, D. T., Po‐Chedley, S., Caldwell, P. M., Ceppi, P., Klein, S. A., and Taylor, K. E.: Causes of higher climate sensitivity in CMIP6 models, Geophysical

811 Research Letters, 47, e2019GL085782, 2020.

812 Zhang, B., Kramer, R. J., and Soden, B. J.: Radiative feedbacks associated with the Madden–Julian
813 oscillation, Journal of Climate, 32, 7055-7065, 2019.

814 Zhang, M. and Huang, Y.: Radiative forcing of quadrupling CO 2, Journal of Climate, 27, 2496-
815 2508, 2014.

816 Zhang, Y., Jin, Z., and Sikand, M.: The top‑of‑atmosphere, surface and atmospheric cloud
817 radiative kernels based on ISCCP‑H datasets: method and evaluation, Journal of
818 Geophysical Research: Atmospheres, 126, e2021JD035053, 2021.

819 Zhou, C., Liu, Y., and Wang, Q.: Calculating the climatology and anomalies of surface cloud
820 radiative effect using cloud property histograms and cloud radiative kernels, Advances in
821 Atmospheric Sciences, 39, 2124-2136, 2022.

822 Zhou, C., Zelinka, M. D., Dessler, A. E., and Yang, P.: An analysis of the short-term cloud feedback
823 using MODIS data, Journal of Climate, 26, 4803-4815, 2013.

824
825
826
827
828

829   **Appendix**
830
831   The ERA5 kernels are computed following Eq. (1) and the approach outlined in Section
832   2.2.
833
834   1. Surface variable kernels
835
836   To execute the partial radiative perturbation computations, the perturbations are prescribed
837   as the following: for the 2D feedback variables, the surface temperature is increased by 1 K and
838   the albedo is increased by 0.01 at each location. Hence, the units of the two kernels, K_{Ts} and
839   K_{ALB} are W m^{-2} K^{-1} and W m^{-2} %$^{-1}$, respectively. When applying them to feedback
840   quantification, their feedbacks are quantified as
841        $\Delta R_{Ts} = K_{Ts} \cdot \Delta T_S$ (A1)
842        $\Delta R_{Alb} = K_{ALB} \cdot \Delta Alb$ (A2)
843   where ΔT_S should be measured in the units of K and ΔAlb in absolute values divided by 1%.
844
845   2. Water vapor kernel
846
847   For the 3D feedback variables, the perturbations are applied to each of the 37 pressure
848   layers (from 1hPa to 1000hPa) and one layer at a time. For the water vapor kernel, a 10%
849   incremental perturbation of the water vapor concentration is used. To adapt to the convention
850   used in the majority of the existing kernels, we convert the units of the kernels to represent the
851   radiative flux change corresponding to an increase of water vapor concentration that conserves
852   the relative humidity of the layer under a 1-K increase in air temperature, i.e., converting the
853   units from W/(m^2 $\Delta q_0^{+10\%}$ 100hPa) to W/(m^2 Δq_0^{+1K} 100hPa):

854        $K_q^{+10\%} = \dfrac{\Delta R_0}{\Delta q_0^{+10\%}}$ (A3)

855        $K_q^{+1K} = \dfrac{\Delta R_0}{\Delta q_0^{+1K}} = K_q^{+10\%} \cdot \dfrac{\Delta q_0^{+10\%}}{\Delta q_0^{+1K}} = K_q^{+10\%} \cdot \dfrac{\Delta q_0^{+10\%}}{q_0} \cdot \dfrac{e_s(T_0)}{e_s(T_0+1K)-e_s(T_0)}$ (A4)

856   Where q_0 is the unperturbed water vapor concentration, in units of kg kg^{-1}. $\Delta q_0^{+10\%}$ is a 10%
857   increment in water vapor concentration. $e_s(T)$ is the saturated water vapor pressure under
858   temperature T, and can be measured by empirical formulas; hence, Δq_0^{+1K} can be measured as
859    $q_0[\dfrac{e_s(T_0+1K)}{e_s(T_0)} - 1]$. Accordingly, when the water vapor kernel is used for water vapor feedback
860   quantification, the feedback is measured as:

861        $\Delta R_q = K_q^{+1K} \cdot \Delta q^{+1K} = K_q^{+1K} \cdot \dfrac{\Delta q}{\Delta q_0^{+1K}} = K_q^{+1K} \cdot \dfrac{\Delta q}{q_0} \cdot \dfrac{e_s(T_0)}{e_s(T_0+1K)-e_s(T_0)}$ (A5)

862   where $\Delta q = q - q_0$ measures the change in water vapor concentration and is normalized by
863   Δq_0^{+1K} to give the factor that is multipliable with the K_q^{+1K} kernel value. If using the Clapeyron-
864   Clausius relation, the above expression can be further approximated as

865        $\Delta R_q = K_q^{+1K} \cdot \dfrac{\Delta q}{q_0} \cdot \dfrac{e_s}{(de_s/dT) \cdot 1K} = K_q^{+1K} \cdot \dfrac{\Delta q}{q_0} \cdot \dfrac{R_v}{L_v} \cdot \dfrac{T_0^2}{1K}$ (A6)

866   where R_v and L_v are the gas constant and specific latent heat of water vapor, respectively. Note
867   that when the kernels are used, T_0 and q_0 typically take their values from the base climate
868   appropriate to the application, e.g., the unperturbed climate of a GCM experiment, not
869   necessarily the dataset used for kernel computation.
870

871   3. Air temperature kernel

872

873   For the air temperature kernel, to be consistent with the "inhomogeneous path treatment"
874   that accounts for the vertically non-uniform temperature distribution within each discrete
875   atmospheric layer (Mlawer et al., 1997), perturbations are added not only to the layer-mean
876   temperature but also the temperature at the exiting boundary of radiative fluxes of interest (i.e.,
877   the upper boundary of each layer for the TOA flux and the lower boundary for the surface flux),
878   to appropriately represent the physical temperature perturbation in each layer.
879   A meaningful test to validate the validity of the air temperature kernel is a vertical sum
880   test, i.e., a linear additivity test to verify the vertical integration of the kernel values reproduce
881   the flux change, either at TOA or surface, in response to a whole-column air temperature
882   increase of 1K. Figure A1 shows that the ERA5 kernel well passes this test. However, as shown
883   by Figure 9, some kernels (e.g., HadGEM3 kernel) show much weaker radiative response at
884   surface, possibly due to improper treatment of the air temperature perturbation in the kernel
885   computation, which may lead to an underestimated air temperature feedback and large biases in
886   the surface feedback analysis.

887
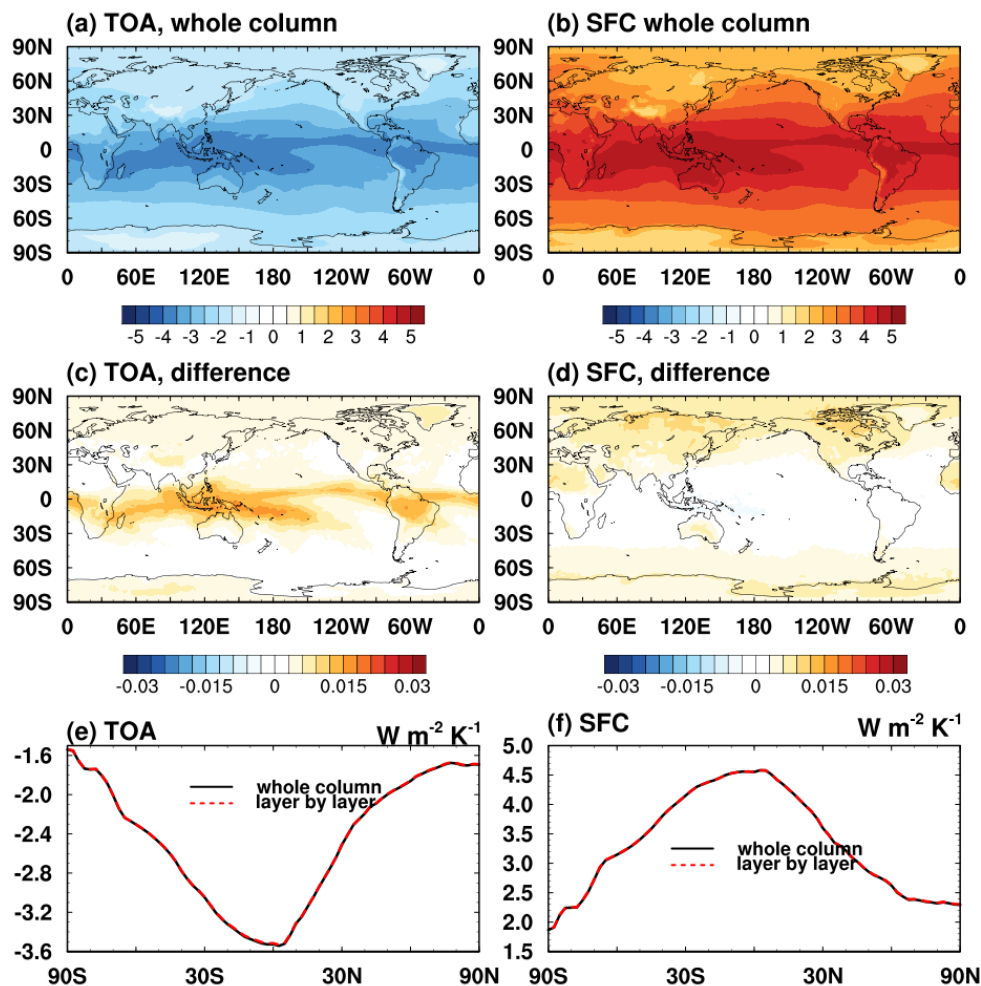
888
889   Figure A1. Monthly mean TOA and surface radiation flux change in response to a +1K
890   air temperature perturbation throughout the vertical column: (a, b) computed by a radiation

891   model, RRTMG; (c, d) difference of vertical sum of air temperature kernels compared to truth in
892   (a, b); (e, f) comparison of the zonal mean.
893

894   Another challenge in the computation of air temperature kernel for surface flux is that the
895   surface in radiative transfer models is also the lower boundary of the lowermost atmospheric
896   layer. If the effects of the surface temperature perturbation on the emission of the surface and
897   that of the lowermost atmospheric layer are not distinguished, this may lead to improper
898   interpretation and use of the surface temperature kernel. In our ERA5 kernel, the two effects are
899   considered separately: according to radiative transfer theory, an increase in surface skin
900   temperature only affects the surface upward emission; an increase in air temperature only affects
901   the downward radiation. In some other kernels such as CAM5, these effects are not
902   distinguished, so that the kernel value represents the net effect, i.e., change in the sum of both
903   downward and upward. As a result, in Figure 10, we see stronger air temperature and surface
904   temperature feedbacks quantified from ERA5 kernels than those from other kernels and in Table
905   S4, we can only report the sum of surface and air temperature feedbacks.
906

907   Figure A2 shows the comparison of vertically integrated air temperature kernels and the
908   sum of surface and air temperature kernels between ERA5, CAM5, HadGEM3 and CloudSat.
909   Although the strength of vertically integrated air temperature kernel for CAM5 is much weaker
910   than that for ERA5 (Figure A2a and b), the sum of surface and air temperature kernel between
911   these two datasets are in good agreement (Figure A2c and d), which warns that the seemingly
912   right temperature feedback quantified by some kernels might come from the misattribution of
913   surface temperature contributions. Another noticeable feature in Figure A2 is that the HadGEM3
914   kernel shows an underestimation in vertical integration of air temperature kernel and an
915   overestimation in the sum of surface and air temperature kernel, likely due to mistreatment of the
916   bottom layer, and this accounts for the biased surface feedback analysis as shown in Figure 9.
917   Similar issues were noticed in Kramer et al. (2019a).
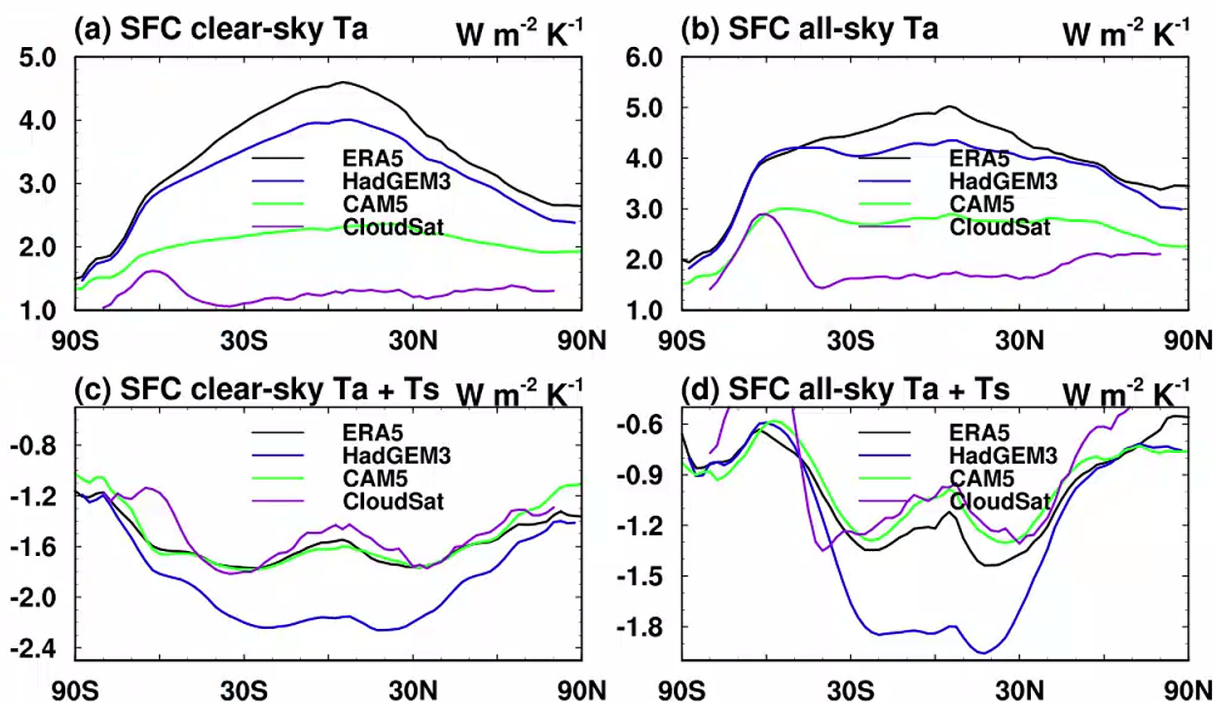
918

919   Figure A2. Comparison of annual mean surface kernels for ERA5, CAM5, CloudSat and
920   HadGEM3 for (a, b) the vertically integrated air temperature kernel values, and (c, d) sum of
921   surface and air temperature kernels.
922
923
924   4. Time averaging
925
926   As described in Section 2.2, all the kernels provided for feedback analysis are averaged
927   from instantaneous kernel values over each calendar month and, in the ERA5 kernel, over
928   multiple years. This is to ensure proper sampling of radiative sensitivity values under different
929   atmospheric states, so that the kernels are representative of mean radiative sensitivity and thus
930   can be readily multiplied with monthly mean climate responses (ΔX) to evaluate climate
931   feedbacks.
932   If the kernels are computed for fixed pressure levels, and if the pressure of any of these
933   levels of an instantaneous atmospheric profile is higher than the surface pressure (i.e., the level is
934   below the surface) at a time instance, this potentially creates inconsistency in the averaging
935   procedure. To address this concern, we set the kernel value to zero (as opposed to missing value)
936   before averaging. This is to ensure that when multiplied with the monthly mean climate response
937   (ΔX), the contribution of a pressure layer (e.g., that centered at 1000 hPa) is effectively counted
938   only for the fraction of time the layer exists (when surface pressure is higher than 1000 hPa).
939   Otherwise, the feedback quantification needs to be further weighted with fraction of time (f)
940   when the pressure layer exists. For example, if the surface pressure is larger than 1000hPa only
941   for half of time in a month (f=0.5), the radiation flux anomaly contributed by the layer centered
942   at 1000 hPa is:
943
944        $\Delta R_{T_{1000hPa}} = K^*_{T_{1000hPa}} \cdot \Delta T_{1000hPa} \cdot f$ (A7)
945
946   Here, $K^*_{T_{1000hPa}}$ represents the kernel value averaged from the time instances when the layer
947   exists. Our averaging scheme is essentially to provide a kernel $K_{T_{1000hPa}} = K^*_{T_{1000hPa}} \cdot f$, so that
948   it can be simply multiplied with $\Delta T_{1000hPa}$ to obtain the same result.
949   Figure A3 illustrates the differences between $K^*_{T_a}$ and K_{T_a}, in terms of their vertically
950   integrated value. Such difference is pronounced over the Southern Oceans (around 60S), where
951   the surface pressure value varies considerably. This likely explains why Figure 3h shows
952   noticeable differences in the air temperature kernel in this region.
953
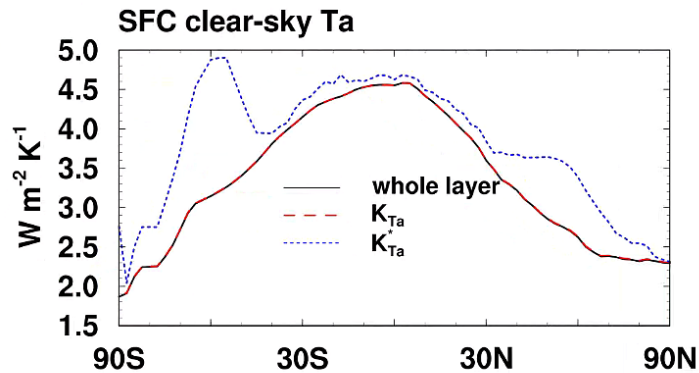
954

955   Figure A3. Zonal mean monthly mean air temperature kernels for surface flux from
956   ERA5 in clear-sky. Black line is the result from the whole column perturbation computation by
957   RRTMG, providing a "truth" for comparison. Red dashed line is the kernel weighted with
958   fraction of time (K_{T_a}) and blue dotted line represents results without weights ($K_{T_a}^*$).
959
960   5. Layer-specified and layer thickness-normalized radiative kernels
961
962   We generate two versions of vertically resolved air temperature kernel, water vapor LW
963   and SW kernel, one with values corresponding to specified vertical layers, i.e., in the units of W
964   m^{-2} K^{-1}, and another with unit-layer thickness (e.g., as shown in Figure 2 and 4), i.e., in W m^{-2} K^{-1}
965   ^{1} 100hPa^{-1}. The latter one properly portrays the vertical distribution of radiative sensitivity to
966   perturbations in unit thickness layers, while the former one may be more convenient to use in
967   feedback quantifications. For TOA budget analyses, these two versions of kernels lead to little
968   difference in practice due to limited contributions from the bottom atmospheric layer. However,
969   for surface budget analyses, we recommend using the layer-specified kernels, as the surface
970   kernels typically show strongest sensitivity to the perturbations in the bottom layers, which can
971   be best accounted for in the non-normalized kernels. Otherwise, the difference of surface
972   pressure between ERA5 and GCMs needs to be carefully treated to avoid errors, for example,
973   caused by missing the radiative contribution from the bottom layer of the atmosphere. To
974   illustrate this issue in an example, consider a location (latitude-longitude grid point) where the
975   surface pressure is 960 hPa in a GCM and the lowermost level of non-zero value of ERA5 air
976   temperature kernel is located at 975 hPa. Had the air temperature change been set to zero or NaN
977   value due to the GCM ground level being above 975 hPa, the contribution to the surface
978   radiation change from the air temperature change in the bottom layer of the atmosphere would
979   not be included, which may lead to a biased quantification of the feedback. We recommend
980   interpolating the air temperature changes from the GCM vertical coordinate to the kernel vertical
981   coordinate, using surface values to replace the missing levels (e.g., the 975 hPa level in the above
982   example) before multiplying with the kernel values, when computing the feedbacks of air
983   temperature and water vapor.
984
985
986
987
988
989
990
991